Reply to the referee comments

Julia Steiner

March 20, 2020

1 Referee 1

General remarks

Dear referee,

thank you for taking the time the review the paper in detail and for giving extensive feedback that helped us improve the draft. An insight from sombody with a more general aerospace based background was very useful for us.

Replies and adjustements to the specific and technical comments are outlined below. With respect to the general comments, most of them are addressed in the specific comments as well. Additionally, I added a couple more references & comparisons to the existing literature: see line 280ff/page 13, line 294ff/page 13, line 352ff/page 16 (expanded below).

- "Comparison with literature: A comparison with the auxiliary slat optimization done by Schramm et al. (2016) and Manso Jaume and Wild (2016) for a 25 % thick base airfoil reveals similar optimal designs. Namely, the obtained slat designs have a large camber, the optimial slat streamwise position aligns with the location of the suction peak on the main element, a stall angle close to 20 degrees and a maximum lift increase of at least 100 %."

- "Nevertheless, despite this somewhat counterintuitive result, the previously mentioned publications (Schramm et al. (2016), Manso Jaume and Wild (2016) and Pechlivanoglou et al. (2010)) use gap width of the same order of magnitude ranging between about 2.5% and 6%."

- "The shape of the optimal main elements is much less sensitive to the aerodynamic efficiency of the design than the optimal shape and position of the slat element. However,this is at least partly a consequence of the structural constraints on the main element, because without the structural constraint especially the pressure side of the main element looked very different. Nevertheless, the main element profiles look very similar to the results obtained by Manso Jaume and Wild (2016)."

Reply to specific comments

page 2, lines 27-43: The described methods for stall delay (vortex generators and Gurney flaps) are not part of the study. It should be checked if this information is of any benefit for the paper.

We consider the benefit of this information the option to highlight that the slat element has a different working principle and can be beneficial for different reasons. Furthermore, the beneficial effects of the two afformentioned elements are more widely known and hence to us it makes sense to mention them.

page 2, lines 47-48: The description of the Circlulation Effect is misleading. The first sentence is not describing the soure of the circulation increase. Instead, the circulation on the rear element induces an upward velocity component at the trailing edge of the preceding element. This has to be compensated by the forward element circulation to achieve the Kutta-condition at the trailing edge.

This was indeed misleading and has been reformulated to: "The circulation around the main element induces an upward velocity component at the slat trailing edge. In order to fullfil the Kutta condition at the slat trailing edge, an increased circulation around the slat is necessary. Thus, the circulation of the slat in the vicinity of the main element is increased as compared to the free-standing slat element only."

page 2, line 51: The description of the Dumping Effect does not describe the origin of the accelerated flow. It must be described that the high velocity at the forward element trailing edge is induced by the low pressure of the suction region at the leading edge of the downstream element.

This was reformulated to: "This effect is closely related to the circulation effect. The circulation around the main element also leads to a low pressure region around the slat trailing edge. As a consequence the high outflow velocity of the boundary layer of the slat relieves the adverse pressure gradient on the slat element. Hence, separation problems are further alleviated."

page 3, line 57/58: It is a misunderstanding that the slat increases the lift coefficient at the same flow condition (angle of attack). This is usually not the case as long as the slat doesnt significantly increase the overall chord length of the airfoil system. This would be accomplished by a steeper gradient oft he lift curve vs.angle of attack. The lift created by the slat compensates the lift drop at the main element due to the reduction of the suction peak (Slat Effect). The part of the statement "an increase of the lift for all angles of attack and" should be deleted. Consequently, the text in the following paragraphs has to be adopted (delete "increased lift and" in line 63 as well as the sentence line 64/65).

The author agrees and this was removed. We do indeed see a lift increase for all angles of attack in our designs, but this seems to be a consequence of the higher apparent chord length.

page 3, line 79: The reference to the airfoil numbers is a correct citation

of the referred work by Pechlivanoglou. Nevertheless, the notation of the TU Delft airfoil deviates from other known notations. Further on, the NACA 22 airfoil is at first not widely known and the notation suggests to be a mistake as there is no 2-digit NACA airfoil series as such. So it would be benefcial to refer to its origin (first named in Weick and Noyes, NACA TN 451, but designed and first tested by Weick and Wenzinger, NACA TR 407)

The additional citation for the NACA-22 airfoil was added. The notation for the TU Delft airfoil was modified from DU97W300 to DU97-W-300 which is the notation used within TU Delft.

page 5, line 131: *Is there an explanation why not a GC2 continuity is targeted. Es- pecially in the leading edge region a curvature continous shape would provide smoother pressure distributions.*

This may be taken into consideration for further publications. Nevertheless, the pressure distribution shown in the paper do not show any irregularities possibly because a smoothing step is performed during the meshing routine. Further, the same shape parametrization was also used by Zahle et al. (2012) and Gaunaa et al. (2012).

page 6, line 147: *Please state what the authors assume to be a "reasonable" mesh resolution in more detail*

The mesh resolution is described later in the article on a case by case basis. For the evaluation of the new designs around 300 points were used along both slat and main element surface, y-plus was kept below 1 and the wall expansion ratios of below 1.2 were used for the structured part of the hybrid mesh.

page 6, line 151: *It is unclear, where a local thickness is imposed.*

The local thickness is defined as the thickness at a specific chordwise station of the profile. It is measured perpendicular to the chord line. The exact location of the local thickness constraints where applied are described later on in the template, namely at 15 % and 40 % chord length.

page 6, lines 161-164: *As the optimization framework and algorithms are not de- scribed in detail, proper reference and citation has to be given.*

Proper citation is given to the GitHub page of the optimization toolbox that is used. A link to the documentation of the toolbox was added in the bibliography. Additionally, a reference to a paper that explains the algorithm is added.

page 7, lines 173-174: *provide citation of the reference to the codes used. For Open- FOAM make sure to refer also the code version and check-out date as opensoure software tends to be changed very rapidly, but the reported results shall be reproducable.*

OpenFOAM-plus, version 1806 was used to obtain the results. For MSES a modified inhouse version was used. The references for OpenFOAM and MSES were already there, but in the fluid model validation section only. These were added in the framework description as well.

page 7, line 176: *Please refer to the airfoil correctly. The airfoil is called NHLP 90 L1T2 (see Woodward Lean, AGARD CP515) and it has been pub-*

lished by Moir as test case A2 for CFD validationdescribed in AGARD AR 303. The correction shall be propagated throughout the manuscript (e.g. page 8, line 201, caption of fig. 4 on page 9)
This has been corrected in the entire draft.

page 7, line 182: *Are the six chord lengths sufficient in the view of the authors to eliminate effects on the boundary condition - or is there a vorticity correction at the farfield boundary employed?*
The sensitivity to the domain size was checked and it was bascially non-existant for the given domain size. Drela himself notes in the MSES manual that: "It must be stressed that the exact values of these grid parameters are not very important, since high-order vortex+doublet farfield representation makes the solution extremely insensitive to the location ofthe outer grid boundaries." A note was added in the revised draft to include the vorticity correction at the farfield boundaries: "The mesh farfield distance was set to six chord lengths around the airfoil and a vorticity correction is used in the farfield."

page 7, line 191: *It is stated that O-mesh topologies are applied although Pointwise is used. Please state, why not a C-mesh is used that would allow an improved capturing of the slat and main airfoil wakes.*
This is a good remark and should be considered in further publications. However, in this paricular case with the automated meshing procedure using an O-mesh was more practical. Further, a thorough mesh sensitivity study was carried out.

page 8, line 200: *The authors suspect the experiment to be the reason for the devia- tions, but it could be the missing resolution of the airfoil wakes, too.*
At this point we cannot rule it out completely, but we have performed simulations on the main element only with an O-mesh at a Reynolds number of 2 million and we were able to match the experimental drag and lift coefficients below stall very well. So it seems unlikely that the O-mesh configuration is causing this large discrepancy.

page 8, line 203/204: *This is a mistake. The Reynolds number in high-lift mulit- element airfoil cases is based on the "clean chord", which is the cruise airfoil with high-lift system retracted.*
This was a mistake in my reporting, because I did not run the simulations myself. I have corrected it in the text after confirming with the coauthor and checking the original paper.
page 8, line 204/205: *This is another - more common - mistake. Although the Mach number is relatively low, a look on the pressure peaks of this case un-veils that the slat suction peak (although not shown here but reported in AGARD AR 303 or AGARD CP 515) gets into sonic speed conditions! Therefore, the choice of an incompressible solver for this airfoil is more than questionable.*
Indeed, the choice of an incompressible solver for this benchmark is not entirely proper. Nevertheless, this is only a validation case and a satisfactory match

4

between experiment and numerical predictions is obtained.

page 8, line 208: The over prediction of the stall angle by 6° seems pretty large as the main motivation of the work is based on the prediction of the stall delay by a slat which is mainly the shift in stall angle.
This is a well known shortcoming of RANS turbulence modeling, but at this point higher-fidelity simulations are too expensive to be used for design cases. Nevertheless, we assume that at least the tendencies - so the sensitivity of lift and drag to changes in the profile shape - are somewhat captured and this is what is important for design optimization.

page 9, line 214: The conclusion that MSES can be used as a substitute for RANS CFD is weak and not supported. MSES is not able to capture confluent boundary layers at all. Due to the small gap and since the optimum slat position is very close to the position where the confluent boundary layer gets dominant (see Woodward and Lean, AGARD CP515, 1993) an optimization procedure neglecting this effect is likely to predict gaps that are too small.
The claim that MES is a substitute is based on empirical observations made here, and is not generalizable to other designs more typical for Aerospace applications, in particular with respect to gap width. We have weaked the statement in the main text a bit. Furthermore, the gap width of the obtained designs tended to converge towards the upper bounds, hence confluent boundary layers are not a concern here (even though MSES can not model them). Plus, we use CFD which can predict confluent boundary layers for the performance assessment post-optimization. So if the optimal gap width obtained from the optimization using MSES was to small, the CFD analysis would make that clear.

page 10, line 223: It is fully unclear why the most sensitive parameter for slat design - the gap - is fixed at the beginning. Additionally, the chosen values seem large. According to Woodward and Lean (1993) an optimum gap is strongly depending on the slat angle and can go down to 2-2.5% chord length. In the further (line 230 and following) the reason for the change in performance is most likely more related to the slat angle than the gap. It is consitent, that the optimal slat deflection angle is lower for the higher gap. At least concerning lift, it does not seem that a maximum lift coeffcient is clearly detected.
Initially, for the preliminary assessment, we also tried to fix the chord length and leave the gap width variable. However, this just resulted in the gap width converging to the upper bound of the gap width. Then, for the actual design cases, the gap width was initially left variable, but the optimal gap width tended to converge to upper bounds as well. Hence, at some point in order to save on computation time it was just left fixed. But we agree, that indeed the gap width chosen for the preliminary optimization are large. Nevertheless, for the actual designs a gap widths of 2 and 4% were used, respectively.

page 10, figure 6: It is not consistent (and not expected by the reader) to show MSES results in these diagrams. Above it was mentioned, that the designs

5

were optimized by MSES but the performance prediction for the evaluation is done with RANS. Especially, there is no clear max. lift coefficient prediction in the shown data.

Since this is only a preliminary assessment neither maximum lift nor RANS results are presented.

page 11, line 258ff: an important description needed to understand the figures and the conclusions should not be placed in an appendix.

The figure was moved into the main text.

page 12, figure 8: This figure is a collection of all optimization data. It is not very explanative as it overlays too much information. It contains already data (of the integral design) that hasnt yet even been introduced and is decribed much later. This figure should be divided for the different design methods and commented accordingly in the text.

The figure contains a lot of information such that comparison between the different configurations and the different design procedures is possible. Hence, we propose to leave the figure as is. But we have added a note in the main text to clarify that some of the information in the figure will be discussed later on.

page 12, lines 263-265: This would be a good option to highlight a common result with previous work (see General comments). This result is also in line with the results obtained by Manso Jaume and Wild for the superimposed slat optimization.

This is a good remark. An additional section was added (already printed in the general remarks section).

page 12, lines 263-265: The statement on the sensitivity of separation on the slat shape is not supported by theory. In constast, a cambered plate is less likely to separate at high angles of attack than a flat plate. Additionally, closing the gap increases the slotted airfoil effects in both directions. In fact, as the slat is moved veritcally, the Slat Effect and the Circulation Effect are expected to get stronger. Only the Dumping effect is expected to be reduced due to the reduction of the suction peak due to the strengthened Slat Effect. In consequence, the slat load is increased (higher circulation and higher trailing edge pressure) resulting in a more cambered airfoil to be more suitable to achieve the circulation without separaton. To verify this, a comparison of the pressure distributions is needed. This conlclusion has therefore to be reworked.

The statement was reworked on (line 287ff, page 13): "Aerodynamic theory indicates that reducing the gap width while avoiding confluent boundary layers leads to an increase in the coupling between the slat and the main element: the slat and the circulation effect are expected to get stronger whereas the dumping effect may be a bit weakened. However, the optimized slat for the lower gap width is less aggressive and the configuration produces less lift, has lower glide ratios and stalls roughly at the same angle of attack. [Nevertheless, this agrees with the literature...]". Indeed, the designs resulting from the reduced

gap width are less aggressive which is contrast to the expected increase in the positive coupling between the slat and the main element. Some remarks about this have also been added in the conclusion. It may be interesting to do further investigation into this in a follow-up study.

page 13, figure 9: *The line legend of figure 9 introduces an undescribed configuration A* in addition (same for fig. 14, and in figs 15-17 configs B*, C*, D*). The meaning and origin is perfectly unclear. It can only be assumed from later reading that this configuration related to the integral design that is described much later (starting from page 15). The pressure distributions shown in the right hand side are not discussed at all in the text.*
The legend text has been adjusted to include also the A* configuration.

page 14, line 298: *To be precise, none of the airofils is optimized for maximum lift coefficient. The airfoil optimization only targeted a high lift coeffciient at a high angle of attack (here AoA=20°). An airfoil stalling at 19° could have a higher max- imum lift coefficient than one not stalled at 20° . To do a maximum lift coefficient optimization it is necessary to detect the naximum lift coefficient of an airfoil by varying the angle of attack.*
The wording has been adjusted to say maximum lift at the design angles of attack.

page 14, line 310: *Here it is stated that experimental data for the clean airfoil would be available for comparison. Such a comparison would have been an asset in section 3.1 regarding the validation of the methodology.*
We already present two validation cases for multi-element airfoils, we consider this to be sufficient for the publication. Otherwise, the length of the paper is excessively increased.

page 15, line 318 *it should be highlighted that - in contrast to the integrated design work of Manso Jaume and Wild, where the suction side contour of the slat is the contour of the original main airfoil - the integral design here is not restricted by the clean airfoil shapein the same way. This underlined the originality of the present work and its relation to previous work.*
The following adjustment was made in the introduction section: Second, the results of an integral design procedure are shown for thick main elements up to 50 % using a variable spline discretization for both the slat and the main element contrary to the simpler parametrization used by [citation].

page 17, lines 334/335: *It is mentioned that the main airfoil shape is a consequence of the structural constraints. But it is more expected that this is an implicit result of the main airfoil shape optimization. Due to the higher curvature, the suction peak is more locally concentrated (improving the Dumping Effect and stabilizing the slat flow) and the trailing edge position therefore placed close to the maximum curvature - which is now much furhter upstream. The intragrated design by Manso Jaume and Wild shows a similar main airfoil*

shape, and there, no structural constraint has been imposed.
While the structural constraints did not have much of an influence on the leading edge and the suction side, the pressure side looked very different without the structural constraints. Namely, the maximum thickness was very far forward followed by a steep decrease in thickness. Hence, we added this remark to the main text. The comparison to Manso Jaume and Wild with respect to the shape of the main element was also added in the main text.

page 17, lines 358-360: The discussion describes a "larger leading edge radius". It would be better to descirbe the leading edge as "more blunt". Further on, it is not a larger leading edge radius that shifts the suction peak to the front. A larger leading edge radius alone would reduce the suction peak but not move it. The present description is misleading as the curvature which is responsible for the interaction with the slat is higher (and the radius smaller) and imposes a reduced pressure at the slat trailing edge.
Indeed, a larger leading edge radius for the same maximum thickness (location) would have been more accurate. We replaced it to say more blunt.

page 17, line 364/365: It is mentioned that the design angle does not account for lower side separation. This is correct, but anyhow, no clear indication of a lower side separation is seen for the designs with slat even at lower angles of attack.
The reasoning there was incorrect. We removed the sentence. Since in fact, the shape of the main airfoil obtained from the integral design procedure are less likely to separate on the pressure side than the aft-loaded reference wind turbine airfoils.

page 17, lines 367/369: This is a very late explanation for a figure that had been placed on page 12. It is necessary to split-up fig. 8 and to place the related illustrations close to the dicsussion in the text.
Again, splitting up the figure makes it more difficult to compare the trends. But as already mentioned we have added some clarification in the main text when the figure first appears.

page 17, lines 371: As already discussed "more rounded" suggests a smoother curvature distribution, while the opposite is the case for the integral designs.
This has been corrected to more blunt.

page 18, lines 374/375 (more likely lines 369/370): This conclusion is in contrast to a previous statement, where it was concluded that the optimal shape of the slat is not as sensitive to the main airfoil optimization and by this not as affected of the auxilary or integral design method (page 17, lines 356/357).
Well, we said the shape of slat is not very sensitive to the main airfoil, the location and to some extent also the orientation is. But we have clarified the

wording on (page 18, line 375-377): "First, the shape of the slat element excluding angle and position is not very dependent on the shape of the main element, but highly dependent on the optimization boundary conditions.".

page 18, lines 383-385: Basically, to show the stalling behavior it is necessary to look at the pressure distribution just at stall onset. Best is a comparison with a very low AoA step before and after maximum lift. The used step of 8° is too large and - depending on the stall onset angle - the stall is developed over the entire configuration but not showing the onset (main wing or slat or both at the same time).
That is why the flow fields are shown in the appendix. However, I added two plots with the pressure and skin friction coefficients in the main text. The following answers will also clarify a bit further.

page 18, line 387: It should be discussed, whether the reattachment due to wake displacement is in accorcance with Sniths 4th effect (Off-Surface Pressure Recovery)
I do not understand your argumentation here, please explain further.

page 18, lines 387-389: As the stall onset is of primary interest, the discussion of the flow fields should not be placed into an appendix.
I left the flow fields in the appendix, but I added two plots with pressure and skin friction coefficients before and after maximum lift in the main text.

page 19, line 393: At least here at the end of all shown pressure distributions, it is necessary to conclude about the suitability of the incompressible solver. Although the flow speed is not mentioned (missing in the case description in Table A.1) the level of the pressure coefficient is less than -15 and imposes the need to check whether this assumption is still valid.
I calculated the free stream Mach number for the NREL 5MW turbine up to about 40 % span and it is below 0.1 which would result in a Glauert correction factor of $c_P/c_{P0} \approx 1.005$. Hence, we did not consider compressible effects, since this is also usually not done for wind energy applications. But I also reran some of the cases with not just accurate Reynolds number, but also accurate Mach number scaling using again the incompressible solver. Then, I checked the maximum Mach number as predicted by the incompressible solver and indeed for the clean cases at angles of attack with lift coefficients above 4, the local Mach number at the slat suction peak approach 0.45, which is not ideal. However, realistically speaking given that RANS overpredicts the stall angle, I don't think that these conditions will actually be reached. Nevertheless, I added this paragraph before the conclusion: "Some of the designs show very high suction peak values for the slat which is an indication that locally compressibility effects may not be negligible despite the low freestream Mach number of $Ma_{\approx}0.1$. Calculating the local Mach number from the incompressible flow field for all the CFD cases shows that for the designs and angle of attack configuration where the lift coefficient is higher than 4 the Mach number locally approach 0.45. This is

9

indeed very high and it is recommended that in future publications, compressibility effects should be considered if a design optimization for high lift is carried out. Nevertheless, given that turbulence model of the CFD solver is expected to overpredict the stall angle, it is not certain that such high Mach number will actually be reached in real life." I also added the freestream Mach number to the table with the design parameters.

page 19, lines 395-397: The description reverses cause and effect. The high suction peak on the main airfoil is the reason for the low trailing edge pressure at the slat - remind Smiths effects.
The sentence was reversed.

page 21, line 428: To conclude on the importance of the gap it should have been used as a design parameter. The limited information on the gap variation (two values only) doesnt allowto draw such abbreviation general conclusion. From other airfoils in literature it is known that the gap is even the most sensitive parameter.
The sentence was modified to: "A reduction in the gap width did not offer any benefits, but only two gap widths were investigated. Possibly, the sensitivity to this parameter warrants further investigation." But as already mentioned, in initial investigation whenever the gap width was left variable the optimal design would converge to the upper bound even when using bounds up to 10 %. Hence, at some point it was fixed to keep structural loading in check. Also, when looking at the references from Manso Jaume, Schramm, Zahle/Gaunaa (also unpublished work), Pechlivanoglou and Schramm gap widths of the same order of magnitude were used (or obtained from optimization).

Reply to technical comments
All the remarks were implemented. With the exception of multi-figure captions as the draft template explicitly asks to remove them. But then later on add them in the full publication. Then the Subsection formation is according to the template guidelines.

2 Referee 2

General remarks

Dear referee,
we appreciate that you took the time to read the paper and give useful feedback that helped us improve the paper. Replies to your remarks follow.

The paper deals with the slat design for thick base profiles at high Reynolds numbers. Due to various combinations of presented cases it is hard to follow the intended logic in the structure. There are too many different cases which are

compared back and forth with references to the appendices. The authors should try to better structure the cases and results. After reading the paper I have a hard time to really summarise it for me with a take home message.

Clarifications in the text have been added to make it more clear. Additionally, some figures and tables have been moved from the appendix into the main text to make easier to understand.

Reply to specific comments

Page 5: *In the shape parametrisation it is written that the leading edge location was fixed to the coordinate system (0,0). Since slat and base profile combined are subject to optimisation it is not clear which leading edge is fixed to (0,0).*

The leading edge of the main element was meant. The text has been modified to clarify this.

Page 6: *The optimisation objectives are formulated as a weighted sum of the performance under clean and rough conditions. What do the authors mean by rough conditions and how do they define it?*

Clean conditions are the conditions where the flow naturally transitions to a turbulence boundary layer. We specify a specific turbulence intensity in the inflow in case of CFD or a specific ampliciation factor in case of MSES which then relates to the transition location. For rough conditions, there is some difference between the results from CFD and MSES. In Mses we specify a specific position on both slat and main element where a transition to a turbulence boundary layer is forced. In CFD, the boundary is assumed to be fully turbulent so there is no transition. Clarification was added to text on page 6.

Page 6: *In eq. 5 and 6 the weighting terms have the index "clean / tripped. So far it is not clear what that means. The authors should give more details on the tripping they applied in their simulations. Also, is only the main profile tripped or also the slat?*

Clarification was added in the text on pages 6 and 7. Both main and slat element are tripped.

Page 8/9: *The authors try to validate their fluid models against different benchmark cases. In the first one they use MSES and CFD and in the second one they use only CFD. They argue that they can use the lower fidelity model for their optimisation procedure as this is only based on the first benchmark. On the contrary, the authors say that the simple model has problems to converge due to the sharp edges in the geometry. This is a limiting factor in their procedure. So why do the authors also show the second benchmark that does not contribute to their decision?*

MSES has been used in literature on cases with sharp edges, but we could not make it work. That is why it was left out. The second benchmark case is used to show that the CFD model can yield accurate drag predictions, because there are issues with this for the first benchmark case. This helps validate our hypothesis that there are issue with the drag measurements for the first benchmark case.

Page 10: *In figure 6 the results for clean and rough are plotted. Again, it is not clear what "rough refers to and how it is defined.*
This should be clear now, since clarification was added on pages 6 and 7. Also see the previous replies.

Page 11, Figure 7: *The caption of the Figure is insufficient, what are e.g. the different lines (dotted,dashed and solid) of the slat?*
The legend has been extended.

Page 12, Figure 8: *What is Lmax, Interm and Gmax? What is the "integral design?*
The integral designs are obtained in an optimization procedure where both the slat and the main element are optimized simulataneously. A remark has been added in the text to say that the results of the integral design procedure are not relevant yet at this point in the text. Lmax, Interm and Gmax refer to the location of the designs on the pareto front as shown in the previous. This figure has been moved from the appendix to the main text, to make it more clear.

Page 13: *Third bullet point: Where is the influence of the base profile thickness discussed?*
It says in the text with respect to the slat design, "The change in the base profile thickness introduces smaller design deviations from the baseline case as compared to the chord and gap width reduction. This goes back to the argument that the strongest design driver for the slat element is the location of the suction peak on the main element."

Page 13: Figure 9: *Again, in the caption is stated "rough and "tripped without any further description.*
This has been explained in previous replies.

Page 14: *Second sentence: What do the authors refer to by stating " Hence, the profiles optimized for maximum lift actually perform worse in terms of maximum lift as compared to the ones optimized for maximum glide ratio ? Where can this be seenin figure 9? Which is the design for lift optimisation and which is the one for maximum glide ratio?*
The legend of Figure 9 has been extended to clarfiy a bit more. What the figure shows is that MSES overpredicts the stall angle and hence the maximum lift as compared to CFD for the cases where we optimized for maximum lift. For the profiles optimized for maximum glide ratio, MSES and CFD predict similar stall angles. Hence, these designs actually yield higher lift.

Page 15, Figure 11 : *insufficient caption.*
The caption has been modified.

Page 17, Figure 13: *What are the differences on the plots? Even the text doesnt help.*

The figure shows the designs resulting from the auxiliary and integral design procedure given the different optimization boundary conditions.

Reply to technical comments

There were only minor remarks and they have been corrected.

Parametric slat design study for thick base airfoils at high Reynolds numbers

Julia Steiner[1], Axelle Viré[2], Francesco Benetti[3], Nando Timmer[4], and Richard Dwight[5]

[1,2,3,4,5]Faculty of Aerospace Engineering, Kluyerweg 1, 2629 HS Delft, Netherlands

Correspondence: J. Steiner (j.steiner@tudelft.nl)

Abstract. Standard passive aerodynamic flow control devices such as vortex generators and gurney flaps have a working principle that is well understood. They increase the stall angle and the lift below stall and are mainly applied at the inboard part of wind turbine blades. However, the potential of applying a rigidly fixed leading edge slat element at inboard blade stations is less well understood but has received some attention in the past decade. This solution may offer advantages not only under steady conditions but also under unsteady inflow conditions such as yaw. This article aims at further clarifying what an optimal two-element configuration with a thick main element would look like, and what kind of performance characteristics can be expected from a purely aerodynamic point of view. To accomplish this an aerodynamic shape optimization procedure is used to derive optimal profile designs for different optimization boundary conditions including the optimization of both the slat and the main element. The performance of the optimized designs shows several positive characteristics as compared to single element airfoils, such as a high stall angle, high lift below stall, low roughness sensitivity and higher aerodynamic efficiency. Furthermore, the results highlight the benefits of an integral design procedure, where both slat and main element are optimized, over an auxiliary one. Nevertheless, the designs also have two caveats, namely a steep drop in lift post-stall and high positive pitching moments.

1 Introduction

Generally, for the inboard part of wind turbines blades, thick airfoils with a high maximum lift and ideally a low roughness sensitivity are preferred over thinner profiles with high aerodynamic efficiency. Further, the installation of vortex generators ahead of the separation line is the current standard in the wind turbine industry (Rooij and Timmer (2003)). This helps delay flow separation to higher angles of attack and compensate for insufficient blade twist. Other flow control devices such as leading edge slats (Zahle et al. (2012); Gaunaa et al. (2012); Schramm et al. (2016)), gurney flaps (Salcedo et al. (2006)) and gurney flaps in combination with vortex generators (Storms and Jang (1994)) have also been considered to enhance the blade performance in the inner third of the blade span.

Generally speaking, stall control methods are more effective than circulation control ones for the inboard blade regions since these blade sections often operate at high angles of attack. Furthermore, given the low contribution to the overall power production of the blades, cost-effective passive methods are more appropriate than active ones.

All of the previously mentioned flow control devices except the leading edge slat have a working principle that modifies the flow near the trailing edge to either increase the stall angle or the lift at the design angle of attack for (quasi-) steady inflow.

Vortex generators introduce a streamwise vortex in the boundary layer. This vortex enhances the mixing of the free-stream flow into the boundary layer and as a consequence makes the boundary layer more robust against adverse pressure gradients. When these small devices with a height of the order of the boundary layer thickness are placed on an airfoil in front of where the separation line would be for the uncontrolled case, the static stall angle is delayed at the cost of a small drag penalty for pre-stall angles of attack (Baldacchino et al. (2016)). Moreover, depending on the exact configuration of the device a very abrupt stall behavior may be observed (Mueller-Vahl et al. (2012)). Several attempts at optimizing the vortex generator shape and placement for static operation point can be found in the literature (Godard and Stanislas (2006); Mueller-Vahl et al. (2012); Fouatih et al. (2016)). Vortex generators are not limited to static stall control but have also been used for dynamic stall control (Pape et al. (2012); Heine et al. (2013); Joubert et al. (2013a, b); Choudhry et al. (2016)). For dynamic stall control, the devices have to be located close to the leading edge such that the formation of the dynamics stall vortex is suppressed or at least delayed to higher angles of attack.

Gurney flaps if applied on the pressure side work by increasing the streamline curvature at the trailing edge and result in an upward shift of the lift curve (Liebeck (1978)). A downward shift of the lift curve is observed if the device is placed on the suction side. Of course, they also introduce a drag penalty which can be managed by appropriately sizing them (Salcedo et al. (2006); Bach et al. (2014)). Due to their location close to the trailing edge gurney flaps have negligible dynamic stall control capabilities (Bach (2016)). Microtabs which are applied close but not directly at the trailing edge exhibit more or less the same characteristics (van Dam et al. (2007)).

By contrast, leading-edge slats are located near the leading edge and have a more complicated working principle than vortex generators and gurney flaps. As Smith (1975) points out the slat does not lead to a blowing type of boundary layer control, but rather a combination of five dominant effects:

– *Slat effect:* The circulation on the slat element leads to a reduction of the pressure peak on the main element.

– *Circulation effect:* The ~~relative positioning between the main and the slat element results in a region of high and downward curved velocity~~ circulation around the main element induces an upward velocity component at the slat trailing edge. In order to fullfil the Kutta condition at the slat trailing edge, an increased circulation around the slat is necessary. Thus, the circulation of the slat in the vicinity of the main element is increased as compared to the free-standing slat element only.

– *Dumping effect:* ~~The~~ This effect is closely related to the circulation effect. The circulation around the main element also leads to a low pressure region around the slat trailing edge. As a consequence the high outflow velocity of the boundary layer of the slat relieves the adverse pressure gradient on the slat element. Hence, separation problems are further alleviated.

- *Off-the-surface pressure recovery:* At least partially, the pressure recovery of the slat wake takes place away from the wall. This type of pressure recovery is more efficient than one in contact with a wall.

- *Fresh-BL effect:* Two fresh boundary layers are formed on both the slat and the main element of the configuration, this increases the resistance of the boundary layer to strong pressure gradients.

As a result of this complex interaction between the two elements, a properly designed slat element leads to ~~an increase of the lift for all angles of attack and~~ a larger static stall angle as compared to the main element alone. However, the slat also has the potential to lead to an increase in drag and a decrease of the lift over drag ratio as compared to the base profile, especially for lower angles of attack.

Smith (1975) also states that for optimal performance of the configuration, the slat trailing edge should be placed and oriented relative to the base element such as to avoid confluent boundary layers.

The ~~increased lift and the~~ higher stall angle ~~make~~ makes slat elements interesting for application at the inboard part of large wind turbine blades for two reasons. First, the high lift configurations would allow for a reduction of the chord length and hence the standstill loads. Second, due to insufficient blade twist, the inboard sections often operate in the post-stall regime. Hence, profiles with higher stall angles have the potential to increase the energy yield of the turbine.

Additionally, experimental investigations into the effect of leading-edge slats under dynamic inflow conditions can be found in literature. They found that a fixed leading edge slat can help ameliorate the effects of dynamic stall for thin profiles as relevant for rotorcraft applications (Carr and Mc Alister (1983); Carr et al. (2001)). The experimental investigation of a VR-7 airfoil with a slat optimized for steady-state operation showed lower peak lift and pitching moment values, as well as, a reduced hysteresis amplitude as compared to the base element only (Carr and Mc Alister (1983)). There are multiple effects at work here - the delayed stall angle and the location of the slat near the leading edge can help suppress the formation of the Dynamic Stall Vortex.

Of course, this is also interesting for wind engineering applications, where the reduction of fatigue loading is important as turbines keep growing in size. In particular, when a wind turbine operates in yaw, the inboard sections often operate under dynamic stall conditions.

While most of the work on slat element design has been done on thin profiles relevant for aerospace purposes, in the past 10 years a few publications tried to assess the potential of such a configuration for thick wind turbine airfoils.

Pechlivanoglou et al. (2010) measured lift and drag on a ~~DU97W300~~ DU97-W-300 base element equipped with a ~~NACA22 slat element. The chord length of the slat element~~ slat element that was 12 % of the chord length of the base element. The slat element in question is the NACA-22 slat, first named by Weick and Noyes (1933), but designed and first tested by Weick and Wenziger (1933). As compared to the base element only, a stall delay of $\Delta_{\alpha_{\mathrm{stall}}} \approx 9°$ and an increase in maximum lift coefficient of $\Delta_{c_L} \approx 1.0$ was observed at a Reynolds number of ~~Re = 1.3m~~ Re = 1.3×10^6.

Zahle et al. (2012) designed and tested a slat element for a 40 % thick flatback airfoil. The main airfoil was a scaled version of the FFA-W3-360 profile. The slat element chord length was 30 % of the chord length of the main element. For the resulting profile, CFD results predicted a stall delay of $\Delta_{\alpha_{\mathrm{stall}}} \approx 16°$ and an increase in maximum lift coefficient of $\Delta_{c_L} \approx 2.5$ along with

3

a decreased roughness sensitivity. Moreover, beyond an angle of attack of $\alpha \approx 4°$ higher lift over drag ratios as compared to the main element were predicted. However, according to CFD results, this was also accompanied by a very steep lift drop post-stall of $\Delta_{c_L} \approx 2.0$ which was however less abrupt in the wind tunnel measurements. Overall, despite the shortcomings of RANS turbulence modeling, the trends observed in the CFD computations agreed with the measurements. Further, the measurements showed strong wall interference effects at high angles of attack rendering the measurement results unreliable.

Later on, Gaunaa et al. (2012) extended the previously mentioned framework to design slat elements for an entire wind turbine blade between 10 % and 30 % blade span. The sectional slat elements were parametrized using Bezier splines, the relative positioning of the slat trailing edge and the slat angle. Subsequently, they assessed the performance of the full, rotating blade with the slat element. ~~The~~ They used the DTU 10 MW reference turbine and simply retwisted the sections where there was overlap with the slat element. Their results showed an increase in the power and thrust coefficient of 1 % and 2 %, respectively. However, the increase in energy yield in the inboard part was accompanied by a decrease in energy yield on the outboard part. Nevertheless, the authors of the paper report an error in the geometry for this publication and hence the results may not be entirely reliable.

Manso Jaume and Wild (2016) designed an optimized slat element for the DU91-W2-250 base profile. Further, they also performed a combined shape optimization of both the slat and the base element for a base profile thickness of 25 % and an optimized slat chord length of roughly 25 % using a steady-state Reynolds-Averaged Navier-Stokes solver with the Spallart Allmaras turbulence model. The integrated design where both main and slat element were optimized showed better performance than the superimposed one in terms of aerodynamic efficiency and slightly less optimal performance in terms of maximum lift. Further, the integrated design was predicted to have a much more docile stall behavior than the superimposed one. ~~Manso and Jaume~~ Manso Jaume and Wild (2016) used a simple parameterization for the slat with six degrees of freedom four of which pertain to the relative positioning of the slat relative to the main element. The remaining two are the slat nose radius and angle. For the parametrization of the base element, three degrees of freedom were allowed, namely suction and pressure side length, as well as, vertical leading edge position.

Along the lines of what has already been done in literature, this study aims to assess the potential of two-element configurations with thick base elements of up to 50 % at Reynolds numbers close to real scale. The article will present a gradual buildup of the optimization complexity by first optimizing only the position of an existing slat element, then optimizing shape and position of an auxiliary slat element, and finally, the integral design approach where slat and main element are optimized simultaneously. The novelty in this article is twofold. First, a detailed analysis of the influence of the optimization boundary conditions on the optimal design is carried out. Second, the results of an integral design procedure are shown for thick main elements up to 50 % using a variable spline discretization for both the slat and the main element contrary to the simpler parametrization used by Manso Jaume and Wild (2016). Both of these aspects have not been discussed in literature before.

2 Optimization methodology

In a review paper on shape optimization for Aerospace applications, Skinner (2018) suggests that the typical design space for these applications show many locally optimal configurations. Hence, global optimization algorithms such as Genetic algorithms or Particle Swarm algorithms seem better suited for these types of problems if a close to optimal configuration is not known a priori. However, global optimizers can be quite inefficient in terms of the number of objective evaluations. This holds true especially towards the end of the optimization, once the approximate location of the local optima is identified. In this stage of the optimization procedure, gradient-based optimizers would be more efficient than non-gradient based ones. Hence, as an alternative a hybrid optimizer can be used. Another option would be to use a surrogate model with a global optimizer.

For the sake of simplicity, in this publication, only a global optimizer in the form of a genetic algorithm is used in combination with a relatively cheap fluid model. Then, for the performance assessment post-optimization a higher fidelity fluid model is used. The different aspects of the optimization framework are summarized in the following:

- **Shape parametrization:** For the parametrization of both the slat and the base airfoil, Bezier spline curves are used. Two splines are used to represent the suction, as well as the pressure side of the profile. Additional constraints are imposed to ensure C0 and C1 continuity between the two sections. The leading edge of the main element location was fixed to the origin of the coordinate system $(0,0)$. A virtual trailing edge point is set at the point $(0,1)$. The trailing edge thickness is then assumed to be perpendicular to the x-axis of the coordinate system and the virtual trailing edge is set to lie in the middle of the trailing edge line. Hence, the chord line always aligns with the x-axis. While, in principle, the trailing edge thickness can be part of the optimization procedure, for this article the trailing edge thickness is fixed.

  For a derivative-free optimization algorithm, the number of spline points should be kept as small as possible to reduce the computational effort. Fitting existing airfoil shapes using six spline points for the suction side and the pressure side gave good results. Due to the geometric constraints at the leading and trailing edge, this leads to thirteen degrees of freedom per element. An example of a spline point distribution and the corresponding profile shape is shown in Figure 1.

  For the representation of the slat position relative to the base element, four degrees of freedom are used. These are: slat chord length c_{slat}, slat chord line rotation β_{slat} relative to the coordinates system of the base element, gap width h_{slat} between the slat trailing edge and the main element, and the surface distance s_{slat} along the base element. The slat coordinate system and scaling are visualized in Figure 1.

- **Fluid models:** The Drela's Integral Boundary Layer (IBL) code MSES and the computational fluid dynamics (CFD) code OpenFOAM OpenFOAM-plus (also abbreviated as OF) are used interchangeably in the optimization framework. The specific settings for the two models will be laid out on a case by case basis in the results section. The mesh for the CFD model is generated automatically. Because of the relatively complicated geometry, a hybrid mesh with structured blocks to resolve the boundary layer around the element is used. With the commercial mesh generator Pointwise, a combination of the hyperbolic extrusion and advancing front algorithms gave reasonable mesh quality.
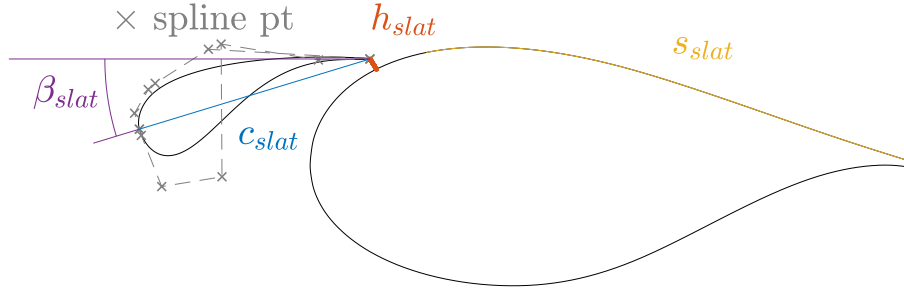
Figure 1. Visualization of the shape paramterization and the slat coordinate system paramterization (adapted from Gaunaa et al. (2012)).

– **Objective formulation and constraint handling** The optimization objectives obj_lift and obj_glide are formulated as a weighted sum of the performance under clean and rough ~~conditions~~condition. The performance under clean conditions respresents the case where natural transition occurs on both elements. Rough conditions assume that the transition is very close to the stagnation point on both elements, depending on the fluid model this is implemented a bit differently and explained in more detail in section 3.1. The performance is evaluated in terms of the normalized lift coefficients $\frac{c_\text{L}}{c_\text{L,ref}}$, as well as, as normalized glide ratios $\frac{(c_\text{L}/c_\text{D})}{(c_\text{L}/c_\text{D})_\text{ref}}$ for three different angles of attack α_j. Hence, a multi-point, multi-objective formulation is employed as written out in Equation 1. The specific objective formulations are given in Equations 5 and 6 where w_x are weighting terms. Additionally, a penalty formulation is used for the constraint handling. Constraints ~~were be~~ are imposed for the local airfoil thickness, the maximum thickness and the (previously mentioned) constraints related to the surface paramterization.

$$\textit{Minimize} \;\; \text{obj}_\text{lift}\left(\mathbf{x}\right), \, \text{obj}_\text{glide}\left(\mathbf{x}\right) \tag{1}$$

$$\textit{subject to} \;\; \text{con}_\text{leq}\left(\mathbf{x}\right) \geq 0 \tag{2}$$

$$\text{con}_\text{eq}\left(\mathbf{x}\right) = 0 \tag{3}$$

$$\mathbf{x}^{(\text{L})} \leq \mathbf{x} \leq \mathbf{x}^{(\text{U})} \tag{4}$$

$$\text{obj}_\text{lift} = \sum_{\alpha_j} \sum_{\text{clean/tripped}\,\text{clean/rough}} w_{\alpha_j} \cdot w_{\text{clean/tripped}\,\text{clean/rough}} \frac{c_\text{L}}{c_\text{L,ref}}(\alpha_j) \tag{5}$$

$$\text{obj}_\text{glide} = \sum_{\alpha_j} \sum_{\text{clean/tripped}\,\text{clean/rough}} w_{\alpha_j} \cdot w_{\text{clean/tripped}\,\text{clean/rough}} \cdot \frac{(c_\text{L}/c_\text{D})}{(c_\text{L}/c_\text{D})_\text{ref}}(\alpha_j) \tag{6}$$

– **Optimization framework:** The Python optimization toolbox Platypus is used which focuses on multiobjective evolutionary algorithms such as NSGAII, NSGAIII, and Particle Swarm optimization. The toolbox also allows for parallel

6

objective evaluation using OpenMPI which was crucial for this project due to the high computational costs. For this study, only the NSGAII algorithm is used. Deb et al. (2002) describe the NSGAII algorithm implemented in the toolbox in detail.

3 Results

Subsection 3.1 will present a validation of the fluid models against experimental benchmark cases. The following three Subsections will highlight the results of three different design approaches: the optimization of the slat position for an existing slat design in Subsection 3.2, the auxiliary optimization of the slat element only in Subsection 3.3 and the integral optimization of the slat and the main element in Subsection 3.4. Finally, a comparison between the designs obtained from the last two design approaches will be presented in Subsection 3.5.

3.1 Fluid model validation

As already mentioned in the previous section, two different-fidelity fluid models are used for the optimization and the performance assessment post-optimization. The lower fidelity fluid model is Drela's commercial IBL code MSES and the higher fidelity model is the open-source CFD code OpenFOAM-plus. In this Subsection, the aim is to present a brief validation of both models on the benchmark case from Pechlivanoglou and Eisele (2014). Additionally, the CFD model will be validated against experimental results from the ~~AGARD A2~~ NHLP-90-L1T2 multi-element airfoil section (Moir (1993)).
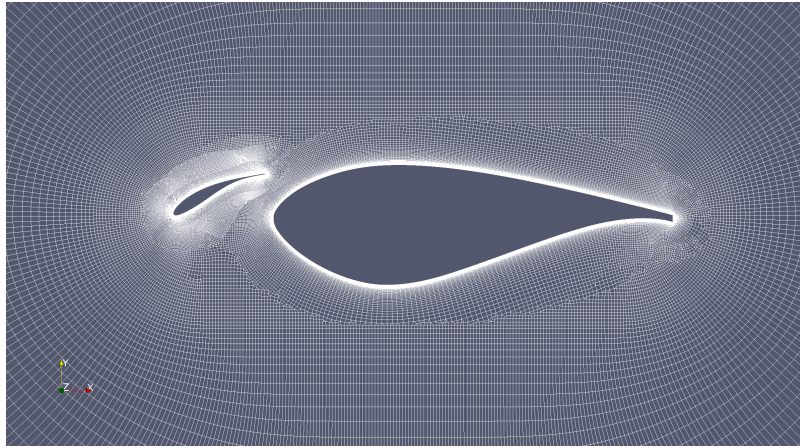
Figure 2. Benchmark configuration with ~~DU97W300~~ DU97-W-300 base airfoil and a ~~NACA22~~ NACA-22 slat element.

The first setup consists of a ~~DU97W300~~ DU97-W-300 base element and a 25 % chord length ~~NACA22~~ NACA-22 slat element (Pechlivanoglou and Eisele (2014)). An illustration of the profile and the CFD mesh are shown in Figure 2. The base element based Reynolds number is ~~Re = 1.3m~~ $Re \approx 1.3 \times 10^6$. The turbulence intensity in the tunnel was around TI $\approx 0.1\%$.

7

MSES solves the Euler equations on a discrete 2D grid, coupled with an integral boundary layer formulation. Transition is predicted by a semi-empirical $\exp^N$ envelope method. Some modifications have been made to this particular version of MSES to improve the stability of the code as detailed in van den Kieboom (2016). The mesh farfield distance was set to six chord lengths around the airfoil and a vorticity correction is used in the farfield. Otherwise, standard grid generation settings were used. To match the turbulence intensity in the wind tunnel the amplification factor was calculated with the correlation $N_{crit} = -8.43 - 2.4 \ln\left(\frac{TI}{100}\right) \approx 8.2$ from Drela (1995). For rough conditions, the boundary layer is tripped for both the slat and the main element at $x/C = 0.1\%$ and $x/C = 10\%$ on the suction and pressure side, respectively.

For the turbulence modeling in OpenFOAM a steady-state Reynolds-Averaged Navier-Stokes (RANS) model is employed. For the ~~fully turbulent cases~~ cases with rough conditions, the k-ω SST RANS turbulence model from Menter (1994) is used. Since this model is fully turbulent, transition does not occur and the boundary layer around the profile is fully turbulent. By contrast, for the cases with natural transition the correlation-based γ-Re_θ transition model from Langrty and Menter (2009) is used as an extension to the original k-ω SST model. Second-order schemes were used for the discretization of the momentum and continuity equations. For convergence reasons bounded first-order schemes were used for the turbulence model transport equations.

For the mesh generation, first cell height fulfills $y^+ < 1$ and the wall expansion ratio is chosen to be $\epsilon_{\text{wall-normal}} < 1.2$. As a result of a mesh convergence study the domain extent of the O-mesh was set to 400 chord lengths and around 300 points were used along the airfoil surface. The mesh is shown in Figure 2. To match the inflow conditions in the wind tunnel experiment, the inflow turbulence was set to $TI = 0.1\%$ and the eddy viscosity ratio was $\nu_t/\nu = 10$.
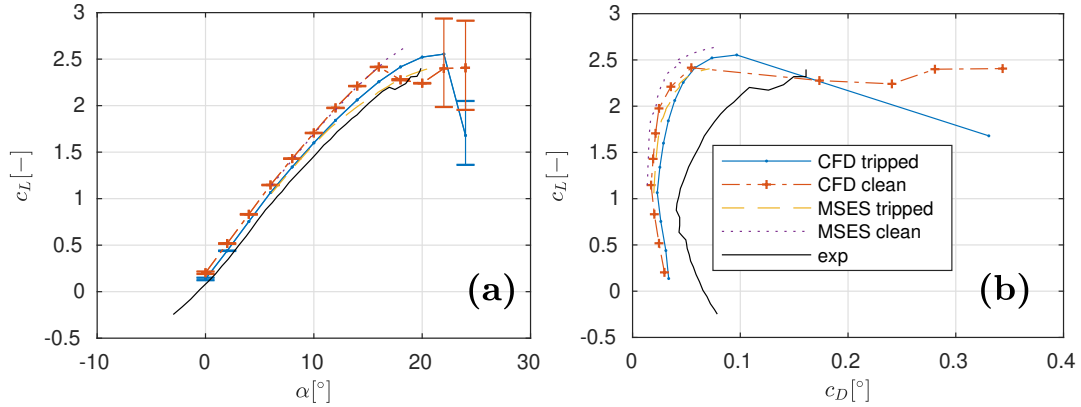
Figure 3. Fluid model validation against the benchmark case from Pechlivanoglou and Eisele (2014) for **(a)** the lift polar and **(b)** the drag polar.

The results from the two models and the wind tunnel measurements are shown in Figure 3. The profile in the wind tunnel was clean, but for the sake of comparison, the tripped configurations are shown in the Figures as well. Close agreement between the lift predictions of MSES and OpenFOAM are observed for both the clean and the rough case. MSES tends to underpredict drag as compared to CFD, but that is expected for IBL formulations. However, both models only yield satisfactory predictions

8

for the lift coefficients and significantly underpredict drag coefficients as compared to the wind tunnel measurements. Because of the close agreement between the two models and because the two codes yielded very accurate results for the base element only, the author speculates that the discrepancy comes either from the experiment description or the experiment itself.
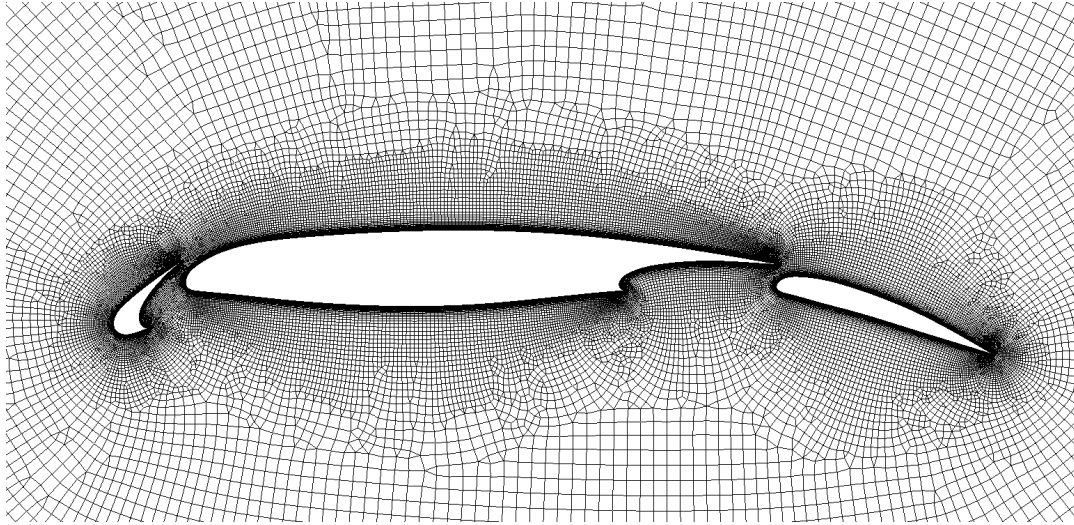

Figure 4. Coarsest considered mesh for the ~~Agard~~ NHLP-90-L1T2 high lift configuration.

215　　Yet, to investigate this discrepancy, the ~~AGARD A2~~ NHLP-90-L1T2 multi-element section from Moir (1993) was considered as a second benchmark case. The profile is pictured in Figure 4. The freestream Reynolds number, Mach number and turbulence intensity corresponding with the experiment are ~~$Re = 3.52m$~~ $Re = 3.52 \times 10^6$, Ma = 0.197 and TI = 0.01%, where the Reynolds number is based on the ~~main element~~ length of the element when slat and flap are retracted. Similarily to Sørensen (2009), given the low freestream Mach number, it can be argued that the use of an incompressible solver is still appropriate.

220 Further, as will be seen later on, good agreement between experimental and numerical results is obtained which confirms the previous hypothesis.

　　The experiment is performed on a clean profile. Nevertheless, both the transitional and the fully turbulent simulations were carried out. The results are shown in Figure 5. The results show an overprediction of the stall angle of about $6°$ and a slight underprediction of the lift and drag below the stall angle. But, overall, the results are satisfactory and show that the employed

225 CFD model is capable of predicting both lift and stall with an acceptable error margin as long as only predominantly attached flow is considered.

　　Unfortunately, MSES would not converge on this benchmark case due to the sharp corners of the profile. Nevertheless, correspondence between the two models was already established in the previous benchmark case. And since both MSES and OpenFOAM capture the same trends in results, it is concluded that for this particular case MSES can be used as a substitute

230 for the higher fidelity CFD model during the optimization procedure.
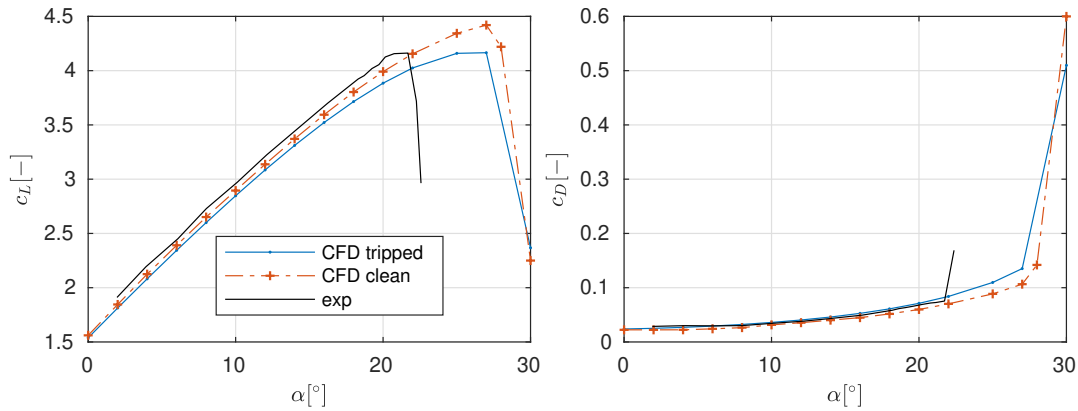
Figure 5. Fluid model validation against the benchmark case from Moir (1993) for (**a**) the lift polar and (**b**) the drag polar.

3.2 Slat dimensioning and optimization settings

The purpose of this Subsection is to establish sensible boundary conditions for the slat dimensions in the two following Subsections. Further, to reduce the computational cost of this step, a preliminary single-objective optimization of the slat position and dimension was carried out. The slat shape was fixed to correspond to the ~~NACA22~~ NACA-22 airfoil. As already

235   mentioned, the slat position and dimension is parametrized using four degrees of freedom: the slat chord length c_{slat} , the slat angle β_{slat}, the distance between the slat and the main element h_{slat} and the streamwise position of the slat element s_{slat}. However, to obtain sensible optimization results, either the slat chord length s_{slat} or the gap width h_{slat} needs to be constrained. Hence, two different fixed wall distances $h_{\text{slat}}/C = 4\%$ and $h_{\text{slat}}/C = 8\%$ were employed. The slat chord length was allowed to vary freely between $15\% \leq c_{\text{slat}}/C \leq 40\%$. The slat angle and chordwise position were not constrained.

240   The local chord-based Reynolds number for the NREL 5MW reference turbine at design conditions was calculated up to 40% span and was found to vary between roughly 9 and 10 million (Jonkman et al. (2009)). Hence, the design Reynolds number for the preliminary, and also the final cases, is chosen to be 10 million. Similarly, the freestream Mach number was also calculated at design conditions and it was below 0.1 up to about 40 % span. Thus, an incompressible CFD solver as custom for wind energy applications was used. However, in MSES compressible effects were considered and hence the freestream Mach

245   number was set to 0.1 when using MSES.

    The results are shown in Figure 6. The outcome shows that, independent of the prescribed slat height h_{slat}, the chord length of the optimal design converges to the upper bound, namely a slat chord length of 40 %. The performance coefficients of the two designs indicate that a larger gap between the slat and the main element also leads to higher lift and lift over drag ratios. However, this comes at the cost of a high positive pitching moment at the quarter-chord point of the main element. Since the

250   slat would have to be attached to the base element, the quarter-chord point of the main element is a logical representative position for the calculation of the combined pitching moment of the profile.
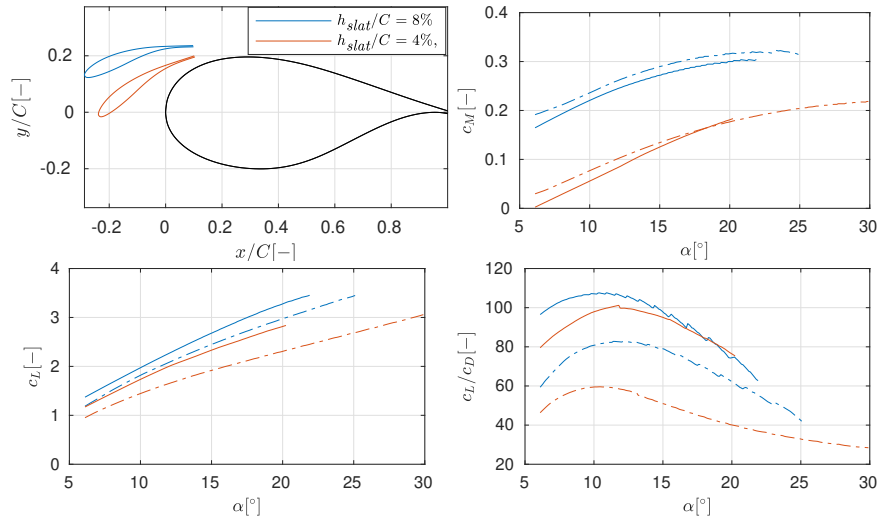
Figure 6. Results of slat position and dimension optimization as estimated with MSES for the clean ($-$) and the rough ($-.$) profile in terms of: **(a)** geometry, **(b)** lift, **(c)** drag and **(d)** pitching moment.

Due to structural considerations, in the remainder, the slat height will be prescribed to be smaller than $h_{\text{slat}}/C < 4\%$. Further, two different chord lenghts will be investigated namely $c_{\text{slat}}/C = 30\%$ and $c_{\text{slat}}/C = 40\%$.

3.3 Auxiliary slat design

255 Now fixing the slat chord length and gap width, the results of the shape optimization of four different auxiliary slat elements are presented in the following. For the optimization, a two-objective formulation is used where the effects of the tradeoff between maximum lift and maximum aerodynamic efficiency are highlighted. Further, three different design angles of attack are chosen, namely $\alpha = 8°$, $\alpha = 12°$ and $\alpha = 20°$, where the second one is weighted the most. Also, the performance of the soiled profile is weighted much higher than the performance of the profile in clean conditions, since the first condition is

260 more prevalent in reality. The general optimization settings ~~are summarized in Appendix ?? in Table ??. The~~ as well as the boundary conditions for the different auxiliary slat designs are specified in ~~Appendix ?? as well in Table ??~~table 1. The choice of boundary conditions documented there will be motivated in the following.

An optimized reference configuration referred to as configuration A with a slat chord length of $c_{slat} = 40\%$, a gap width of $h/C = 4\%$ and a base profile thickness of $t_{max}/C = 40\%$ is chosen. The base profile has the shape of the DU00-W2-

265 401 profile. At this point, no structural constraints are considered. Hence, the only constraint that is imposed on the slat geometry is that, at each chordwise position, the thickness is larger than the trailing edge. The trailing edge thickness is fixed to $h_{TE,slat}/C = 0.2\%$.

To assess the influence of the gap size between the slat and the main element, the slat relative chord length and the base profile thickness on the optimal slat design, the optimization procedure is also carried out for three modified design. For the

11

Table 1. General optimization settings (left) and optimization boundary conditions for the auxiliary slat design (right).

Classification	Parameter	Value
Flow regime	Reynolds number	10 million
	Mach number	0.1
	Amplification factor	2
NSGAII settings	Nr of design vars	15
	Mutation rate	$0.02 - 0.05$
	Crossover rate	0.8
Objective weighting	α_j	$[8.0°, 13.0°, 20.0°]$
	w_{α_j}	$[0.6, 1.0, 1.0]$
	$w_{clean}, w_{tripped}$	$[0.2, 0.8]$

Classification	Parameter	Value
Conf. A	Base profile	DU00-W2-401 (DU40)
	Slat chord c_{slat}/C	40%
	Gap width h_{slat}/C	4%
Conf. B	Base profile	DU00-W2-401
	Slat chord c_{slat}/C	40%
	Gap width h_{slat}/C	2%
Conf. C	Base profile	DU00-W2-401
	Slat chord c_{slat}/C	30%
	Gap width h_{slat}/C	4%
Conf. D	Base profile	FFA-W3-480 (FFA48)
	Slat chord c_{slat}/C	40%
	Gap width h_{slat}/C	4%
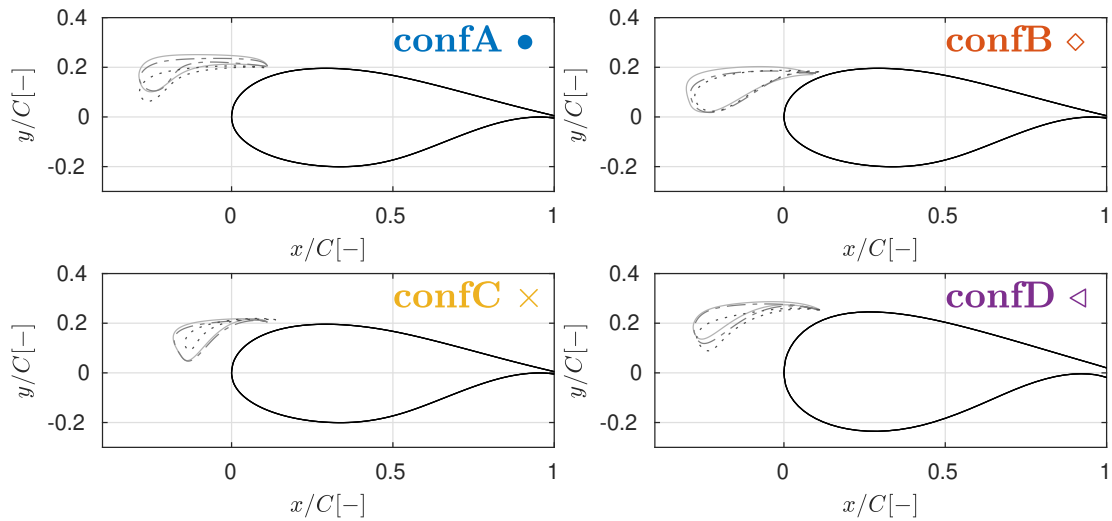
Figure 7. Designs obtained using the auxiliary design procedure optimized for maximum lift $(-)$, maximum glide ratio $(:)$ and a combination of both $(-.)$, see figure 8 for clarification.

second configuration named configuration B, the gap size is halved to $h/C = 2\%$ as compared to the reference design. For the third configuration referred to as configuration C, the slat chord length is reduced from $c_{slat}/C = 40\%$ to $c_{slat}/C = 30\%$. Lastly, for the fourth design named configuration D, a thicker base profile with a thickness of $t_{max,base}/C = 48\%$ is chosen. The base profile is a scaled version of the FFA-W3-360 profile which was used in the The DTU 10MW Reference Wind Turbine Project Site.
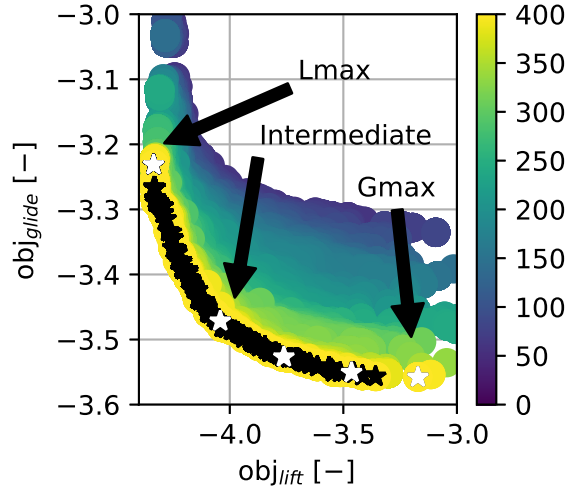
Figure 8. Pareto front example for the two-objective optimization with annotation of the two extreme and the intermediate objects. The color bars refers to the generation of the population.

The optimal slat designs are pictured in Figure 7. Each time, three points on the Pareto front are shown. The three points correspond to the two extreme points and one point roughly in the middle of the Pareto front. For clarification see the example shown in ~~Appendix ??~~figure 8. Figure 9 compares the different optimal slat designs in terms of slat angle, thickness, camber, and streamwise position. The figure also already contains the results from the integral design procedure that will be presentend later on, so for now part of the results can be ignored.

Given the limited sensitivity analysis shown in Figures 7 and 9, the following observations can be made:

– *General trends:* The optimal slat design for all configurations and objective weightings are highly cambered, with cambers of the shown designs ranging between roughly 8% and 20%. This is a consequence of the previously mentioned dumping effect. Due to this, attached flow around the slat can be maintained even for a highly cambered profile. Moreover, the chordwise positioning of the slat is largely insensitive to the imposed design choices. The optimal streamwise position of the slat relative to the base element is mostly determined by the streamwise location of the suction peak on the base element. Since all the base profiles are classical thick wind turbine airfoils, the location of the suction peak is very similar. Namely, the profiles have a ~~rounded~~ relatively blunt leading edge that is designed to have the transition point close to the airfoil nose. Hence, the optimal streamwise slat position is around $x_{\text{TE,slat}}/C \approx 10\%$ for all the investigated constellations. As compared to more traditional high lift configurations for aerospace applications, the streamwise location of the slat element is further aft. This is, because usually for aerospace applications, thinner profiles which have the suction peak further forward are used.

13
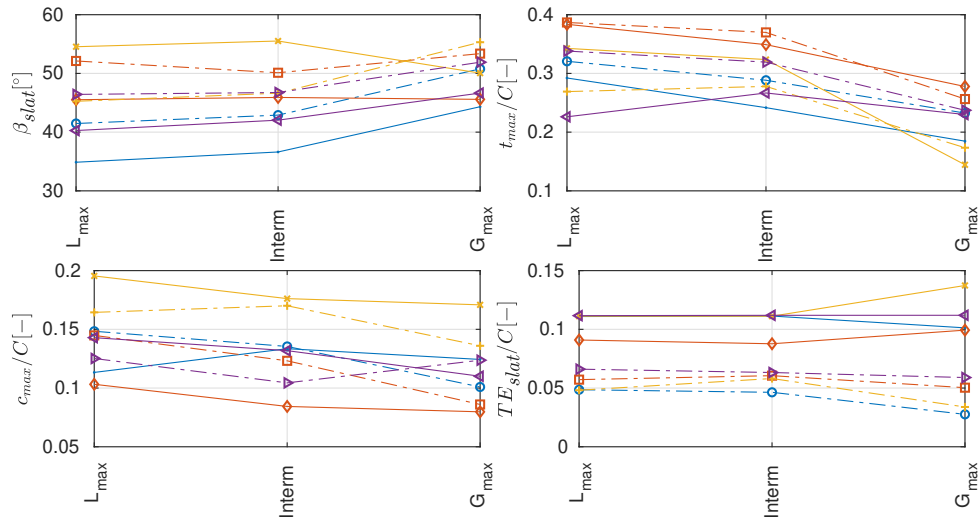
Figure 9. Slat characteristics from the auxiliary (−) and the integral (−.) design procedure in terms of **(a)** slat angle, **(b)** slat thickness, **(d)** slat camber, and **(d)** slat streamwise trailing edge location.

- *Comparison with literature:* A comparison with the auxiliary slat optimization done by Schramm et al. (2016) and Manso Jaume and Wild (2016) for a 25 % thick base airfoil reveals similar optimal designs. Namely, the obtained slat designs have a large camber, the optimial slat streamwise position aligns with the location of the suction peak on the main element, a stall angle close to 20 degrees and a maximum lift increase of at least 100 %.

- *High lift versus high glide performance:* With exception of the design with the reduced chord length, the trade-off between high lift and high glide performance leads to smaller differences in the optimal designs than the change of the optimization boundary conditions. Except for one outlier, thinner and less cambered designs correlate with higher aerodynamic efficiency of the whole profile.

- *Influence of the gap width:* The reduction of the gap width between the slat and the main element leads to more downward turned, significantly thicker and less cambered optimal slat designs as compared to the baseline designs. ~~Both the~~ This quite marked trend was also observed in other preliminary, unpublished designs (not shown here) with base airfoil thickness ranging between 25 % and 40 %. Aerodynamic theory indicates that reducing the gap width while avoiding confluent boundary layers leads to an increase in the ~~slat angle and the decrease in the slat camber lead to slat designs which are less likely so separate at higher angles~~ coupling between the slat and the main element: the slat and the circulation effect are expected to get stronger whereas the dumping effect may be a bit weakened. However, the optimized slat for the lower gap width is less aggressive and the configuration produces less lift, has lower glide ratios and stalls roughly at the same angle of attack. ~~This indicates that reducing the gap width weakens the positive interaction between the slat and the main element. The influence on the slat thickness has been observed in other preliminary designs as well.~~ Nevertheless, despite this somewhat counterintuitive result, the previously mentioned

14

- *Influence of the slat chord length:* The curtailment of the slat chord length leads to much higher cambered slat designs as compared to the baseline profiles. The higher camber indicates that a strong positive coupling exists between the slat and the main element since such a highly cambered profile would separate at fairly low angles of attack if used alone. The design optimized for maximum lift does not seem realistic and is solely exploiting a weakness of the fluid model. This will be further explained later in the article.

- *Influence of the base profile thickness:* The change in the base profile thickness introduces smaller design deviations from the baseline case as compared to the chord and gap width reduction. This goes back to the argument that the strongest design driver for the slat element is the location of the suction peak on the main element.
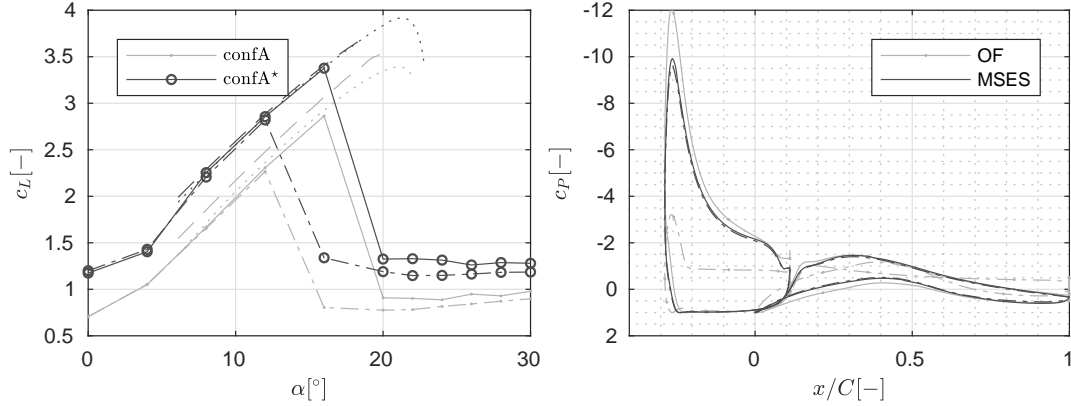
Figure 10. Performance assessment of ~~two designs~~ configuration A cases optimized for maximum lift ~~through~~ using either the auxiliary (caseA) or the integral design (caseA*) procedure. Shown in the figure are **(a)** the lift polar and **(b)** the pressure distribution at $\alpha = 16°$ as obtained using OpenFOAM ($-$ clean, $-.$ rough) and MSES ($--$ clean,$\cdot\cdot$ tripped).

Moving on to a more detailed performance assessment of the optimal designs, the performance coefficients the maximum lift and the maximum glide ratio designs as estimated by CFD are shown in Figures 10 and 11, respectively.

Figure 10 shows a comparison between the lift predictions from MSES and OpenFOAM for the baseline configuration alongside the pressure distribution at $\alpha = 16°$. As was previously alluded to, the optimizer seems to exploit weaknesses in the fluid model for the high lift designs. Due to the setup of the optimizer, the flow model has to converge up to $\alpha = 20°$. However, MSES tends to overpredict the stall angle by at least $\Delta_\alpha \approx 5°$ as compared to OpenFOAM. Further, as was already visible in the benchmark cases, the employed turbulence models for CFD do already overpredict the stall angle as compared to measurements. For the rough profile at $\alpha = 16°$, MSES predicts fully attached flow on both elements whereas OpenFOAM seems to indicate large separation zones on both elements. Hence, the profiles optimized for maximum lift at the design angles

330 actually perform worse in terms of ~~maximum~~ lift as compared to the ones optimized for maximum glide ratio <u>at the design angles</u>. Thus, going forward only the designs optimized for maximum glide ratio will be considered. Due to the shortcomings of MSES in modeling the stall onset, it does not seem to be a suitable tool to be used in maximum lift design optimization. For the sake of completeness, the lift and drag polars for the high lift designs are plotted in Appendix A in Figure A1.
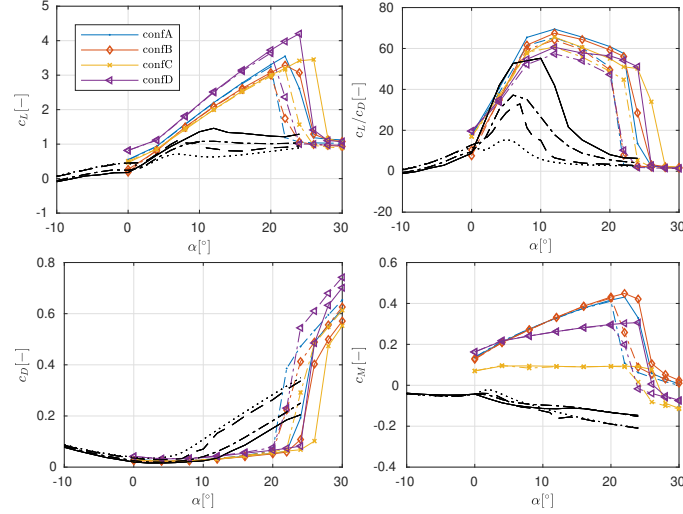

Figure 11. Lift **(a)** and drag **(b)** polar from CFD for the slat configurations optimized for maximum aerodynamic efficiency using the auxiliary design strategy, the coefficients for the clean $(-)$ and tripped $(-.)$ DU40 profile only, as well as, the clean $(--)$ and tripped $(\cdot\cdot)$ FFA48 base profile only are shown as well.

The performance of the profiles optimized for maximum glide ratio in Figure 11 shows some common characteristics despite
335 the different optimization boundary conditions. For the rough profiles, the stall angle lies close to $\alpha \approx 20°$ and maximum lift coefficients lie above $c_L > 3$. Beyond stall the lift coefficients steeply drop to $c_L \approx 1$. The roughness sensitivity is strongly reduced as compared to the base profile only, but this could also be a consequence of the low weighting of the clean performance in the objective formulation. Beyond $\alpha \approx 8°$, the glide ratio is larger than for the base profile only and the glide ratio shows a much less pronounced peak in the glide ratio distribution. The combined pitching moment calculated at the quarter chord point
340 of the main element is positive due to the forward location of the slat element. The force and momentum coefficients for the main element only, shown in Figure 11, are obtained from CFD as well, even though measurements are available.

As compared to the baseline design, both a reduction in the gap between the main and the slat element, as well as a curtailment of the slat chord length, lead to lower lift and lift over drag values. As expected, an increase in the base element thickness leads to higher lift and drag coefficients. The largest spread in the performance coefficients between the different designs is
345 seen in the pitching moment coefficient. The design with the curtailed chord length shows pitching moment coefficients of the same magnitude as the main element only. The pitching moment of the other designs is between 2 and 4 times higher than that of the base element only.

Table 2. General optimization settings (left) and optimization boundary conditions for the integral slat design (right).

Classification	Parameter	Value
Flow regime	Reynolds number	10 million
	Mach number	0.1
	Amplification factor	2
NSGAII settings	Nr of design vars	28
	Mutation rate	$0.02 - 0.05$
	Crossover rate	0.8
Objective weighting	α_j	$[8.0°, 13.0°, 20.0°]$
	w_{α_j}	$[0.6, 1.0, 1.0]$
	$w_{clean}, w_{tripped}$	$[0.2, 0.8]$

Classification	Parameter	Value
Conf. A*	Base profile thickness t_{max}/C	40%
	Slat chord c_{slat}/C	40%
	Gap width h_{slat}/C	4%
Conf. B*	Base profile thickness t_{max}/C	40%
	Slat chord c_{slat}/C	40%
	Gap width h_{slat}/C	2%
Conf. C*	Base profile thickness t_{max}/C	40%
	Slat chord c_{slat}/C	30%
	Gap width h_{slat}/C	4%
Conf. D*	Base profile thickness t_{max}/C	48%
	Slat chord c_{slat}/C	40%
	Gap width h_{slat}/C	4%

3.4 Integral design of slat and main element

In this subsection, the results of an integral slat design procedure where both the shape of the main and the slat element are optimized simultaneously will be presented. Again, four different cases with the same boundary conditions as for the design of an auxiliary slat design will be used. ~~Hence, the reader is again referred to Table ?? for a summary of the~~ The general optimization settings and ~~Table ?? for the boundary conditions.~~ the optimization boundary conditions are summarized in table 2.

The fixed trailing edge thickness of the slat element remains unchanged. The trailing edge thickness of the main element is fixed to $h_{TE}/C = 1\%$. Additionally, to make the design more realistic additional thickness constraints are imposed on the main element. This is to ensure that there is enough space for the wing box. Analogous to Bak et al. (2014), a minimum local thickness of $t(x/C)/t_{max} > 85\%$ was enforced at two chordwise stations, namely at $x_1/C = 15\%$ and at $x_2/C = 40\%$. This leaves space for a box length and height of at least $l_{box}/C = 25\%$ and $h_{box}/t_{max} = 85\%$, respectively. For the design of the slat element structural constraints are ignored at this point since they are considered less critical because both the bending and the torsional loads on the slat element are lower than the loads on the main element.

The resulting optimal designs are shown in Figure 12. Again three elements of the Pareto front are shown, the two most extreme ones and one roughly in the middle. At first sight, the designs look very similar to the ones from the previous Subsection where only the slat element is optimized. The optimal slat designs show the same sensitivity to the boundary conditions as for the design in the previous Subsection. However, their streamwise placement is much further forward than for the auxiliary slat design cases owing to the ~~larger leading edge radius~~ blunter leading edge of the main elements. The shape of the optimal main elements is much less sensitive to the aerodynamic efficiency of the design than the optimal shape and position of the

slat element. However, this is at least partly a consequence of the structural constraints on the main element, because without the structural constraint especially the pressure side of the main element looked very different. Nevertheless, the main element profiles look very similar to the results obtained by Manso Jaume and Wild (2016). A more detailed comparison between the designs obtained with the auxiliary and the integral design procedure will be shown in the next Subsection.
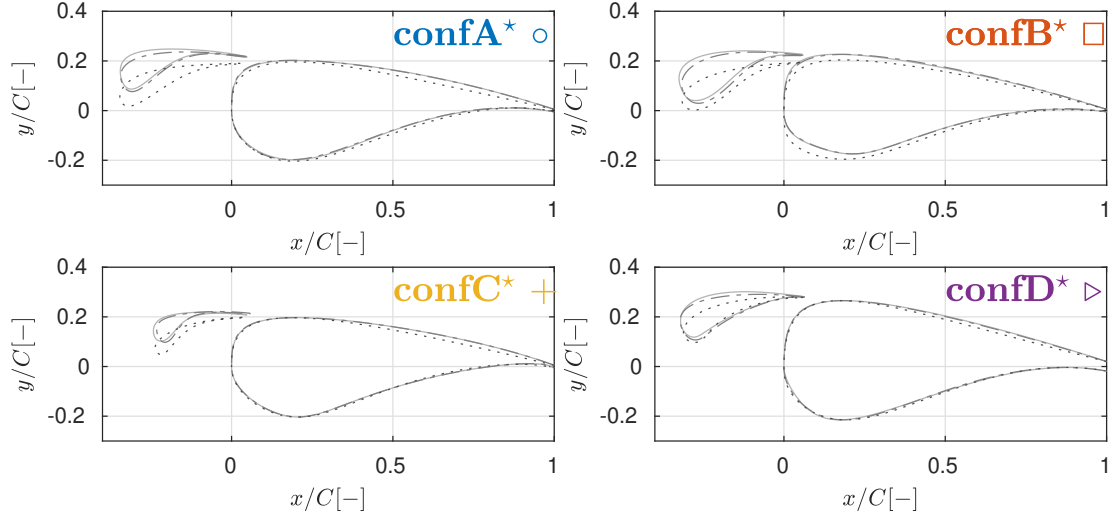

Figure 12. Designs obtained using the integral design procedure optimized for maximum lift ($-$), maximum glide ratio (:) and a combination of both ($-.$), see figure 8 for clarification.

The performance assessment of the optimal designs was again carried out using CFD. The result for the designs with the maximum glide ratio are shown in Figure 13. Since the designs optimized for maximum lift suffer the same shortcomings as for the previous optimization round, they are not discussed and only pictured in Figure A2 in Appendix A.

Again also the integral two-element designs optimized for maximum aerodynamic efficiency show some common characterictics. The stall angle lies around $\alpha \approx 25°$ and a steep drop in the lift coefficient to about $c_L = 1.5$ is predicted post-stall by CFD. The glide ratios lie above the ones for the main element only for $\alpha > 8°$. For some of the designs, this holds true even below that angle of attack. The glide ratio remains close to the maximum glide ratio for the angle of attack range of roughly $8° < \alpha < 20°$. Further, a much lower roughness sensitivity than for the base element only is observed. Lastly, again the pitching moment coefficients show the largest dependence on the optimization boundary conditions.

When comparing with the performance of the designs with the fixed main element from Figure 11, roughly the same sensitivity to the boundary conditions is observed and some performance gains are obtained through a more integral design approach independent of the boundary conditions. Namely, the stall angle increases by about $\Delta_{\alpha_{stall}} \approx 5°$. Further, at $\alpha = 20°$, an increase in lift coefficient and aerodyanmic efficiency of at least maximum $\Delta_{c_{Lmax}} \approx 0.5$ and $\Delta_{G_{max}} \approx 5$ is observed, respectively. On the flipside, due to the higher lift also the pitching moment increases, at $\alpha = 20°$, the pitching moment increases by about a factor of two for all the designs.
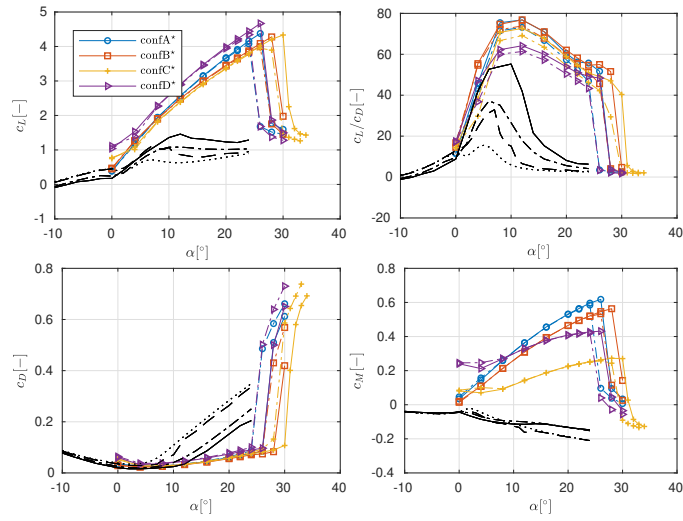
Figure 13. Lift **(a)** and drag **(b)** polar from CFD for the slat configurations optimized for maximum aerodynamic efficiency using the integral design strategy, the coefficients for the clean (−) and tripped (−.) DU40 profile only, as well as, the clean (−−) and tripped (··) FFA48 base profile only are shown as well.

3.5 Comparison between designs with integrated and auxiliary slat design

In this Subsection, a more detailed comparison between the optimal designs from the auxiliary slat and the integral two-element procedure is presented.
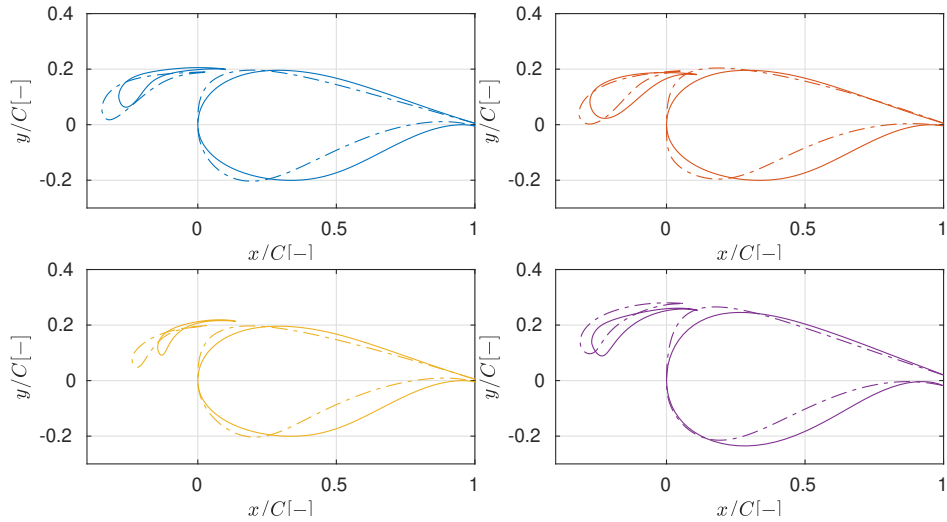
Figure 14. Comparison of profiles obtained using the auxiliary (−) and the integral (−.) design procedure.

Figure 14 shows the designs optimized for aerodynamic efficiency for the auxiliary and the integral runs. Three general trends are observed when comparing the integral with the auxiliary designs independent of the boundary conditions. First, the shape of the slat element excluding angle and position is not very dependent on the shape of the main element, but highly dependent on the optimization boundary conditions. Second, the optimal main elements show a much ~~larger leading edge radius~~ blunter leading edge and a lower profile thickness beyond $x/C \approx 35\%$ as compared to the standard wind energy airfoils used for the auxiliary slat design. The ~~larger leading edge radius~~ blunt leading edge leads to a forward shift of the suction peak, and hence, a forward shift of the optimal slat position as compared to the fixed main airfoils. The thinner shape of the ~~profiles~~ main elements for the backward part of the profile ~~potentially has two origins. First, it could be a consequence of the thickness constraints related to the box length. An increase in the hypothetical box length will lead to a higher thickness in the backward part of the airfoil. Second, out of the three design angles of attack, the lowest one was set to $\alpha = 8°$. Such a high minimum design angle does not consider the flow separation present on the pressure side for smaller angles of attack. However, this is not a problem, since these profiles would be used in the inboard part of a full rotor blade where higher inflow angles are expected~~may be a result of different wing box constraints, namely for the design of the wind turbine base airfoils possibly a larger box length was assumed. A more cambered main element leads to higher lift from the main element only which allows for less aggressive slat designs for the same total lift between main and slat element and higher stall angles.

In Figure 9, the slat angle, thickness, camber, and streamwise trailing edge location are shown both for the auxiliary and the integral design procedure. The two extreme elements and one element roughly from the middle of the Pareto front are shown. The range of the optimal slat thickness and camber is not strongly influenced by the choice of the design procedure. The slat angle and streamwise trailing edge location are more dependent on the choice of the design procedure. As already mentioned, the ~~more rounded~~ blunter leading edge of the main elements resulting from the integral design procedure leads to a more forward optimal slat trailing edge position. Additionally, the range in the optimal slat angle roughly halves when compared to the auxiliary design procedure. Likely, because a more forward position of the slat element reduces the influence of the shape of the base element on the optimal slat design.

In Figures 15, 17, 18 and 19 the pressure distributions for three angles of attack are shown for the designs optimized for maximum aerodynamic efficiency resulting from both the auxiliary and the integral design procedure. The pictured angles of attack are the two design angles $\alpha = 12°$ and $\alpha = 20°$, as well as an angle $\alpha = 28°$ that is either close to stall or post-stall, depending on the design.

For the two baseline designs shown in Figure 15, the profile resulting from the auxiliary optimization procedure shows higher suction peaks on the slat element and lower suction peaks on the main elements for all the pictured angles of attack as compared to the profile resulting from the integral design procedure. This shows that the integral design procedure leads to profiles which better balance the inverse pressure gradients on the two elements. Hence, the flow around the resulting designs is expected to remain attached up to higher angles of attack.

Both profiles also show the same stalling behavior ~~. In fact, this is observed for all the designs optimized for maximum aerodynamic efficiency in this article~~as visualized in figure 16 for the clean reference configuration obtained from the integral design procedure. Initially, simultaneously the flow on both the slat and the main element begins to stall from the trailing edge.
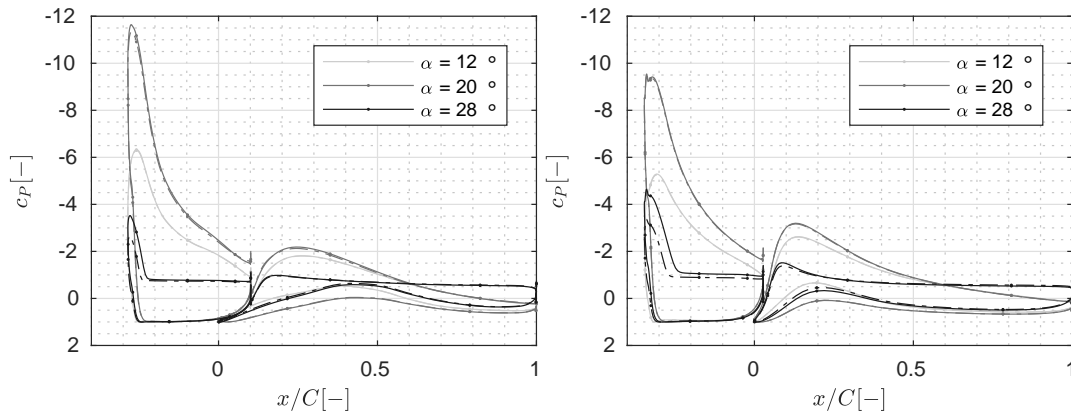
Figure 15. Pressure distribution from CFD for: the clean (-) and the rough (-.) profile at different angles of attack for **(a)** configuration A, and **(b)** configuration A*.
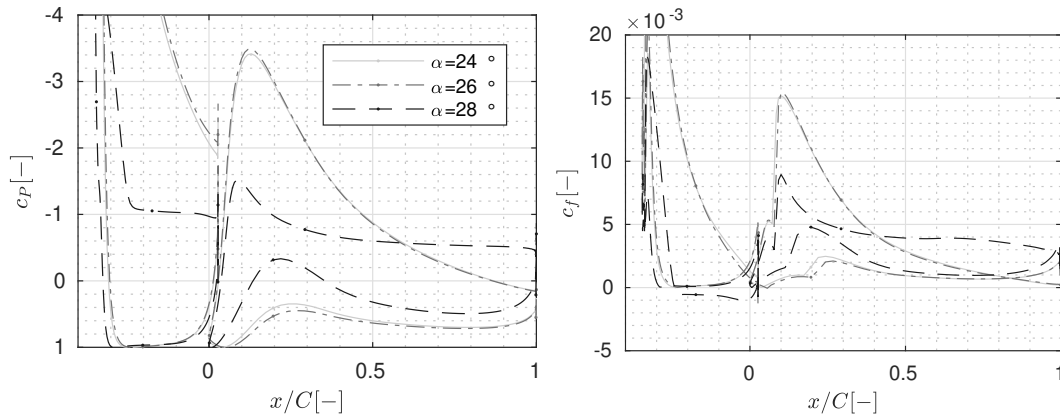

Figure 16. Stall progression for configuration C* optimized for maximum glide ratio from CFD for the clean configuration: in terms of **(a)** pressure, and **(b)** skin friction coefficients

As the angle of attack is further increased and the separation line moves towards the leading edge, the wake of the slat becomes
425 wider as well. At some point, the slat wake extent grows so much that the low-pressure area in the wake leads to reattachment of the flow on the main element. Finally, at some point, both elements are fully separated. In fact, this is observed for all the designs optimized for maximum aerodynamic efficiency in this article. See the Figures B1 and B2 in Appendix B for a visualization of this process for the configuration with the reduced chord length.

For the profiles with the smaller gap width shown in Figure 17, the pressure distributions look very similar to the baseline
430 case. The main difference is that for these two configurations, the slat is turned into the flow a bit more. As a consequence, the lift is a bit lower and the stall angle a bit higher as compared to the baseline design.
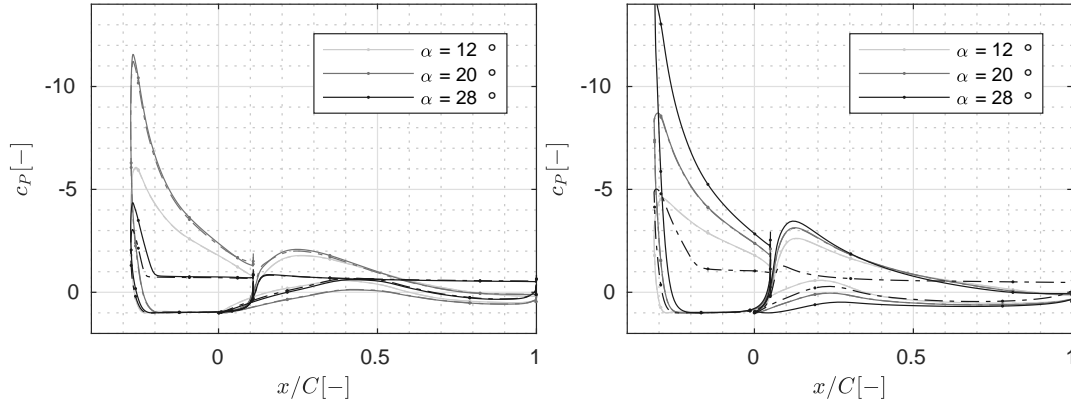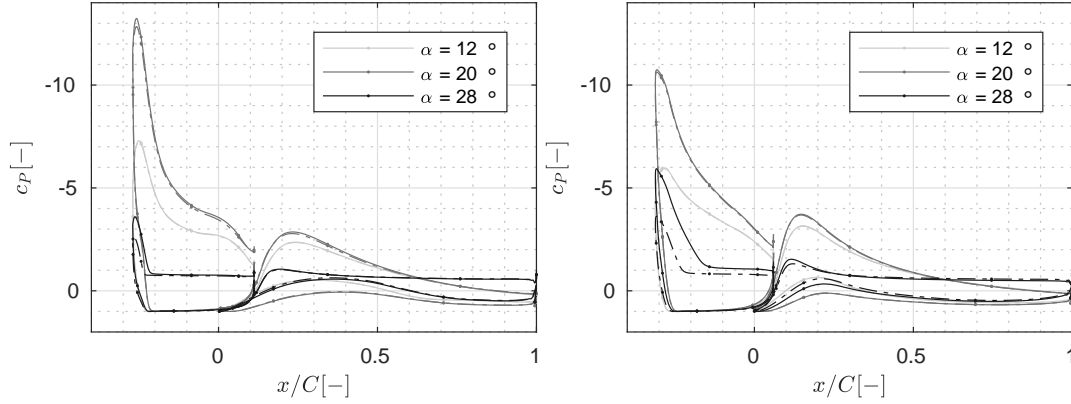
Figure 17. Pressure distribution from CFD for: the clean ($-$) and the rough ($-.$) profile at different angles of attack for **(a)** configuration B, and **(b)** configuration B*.
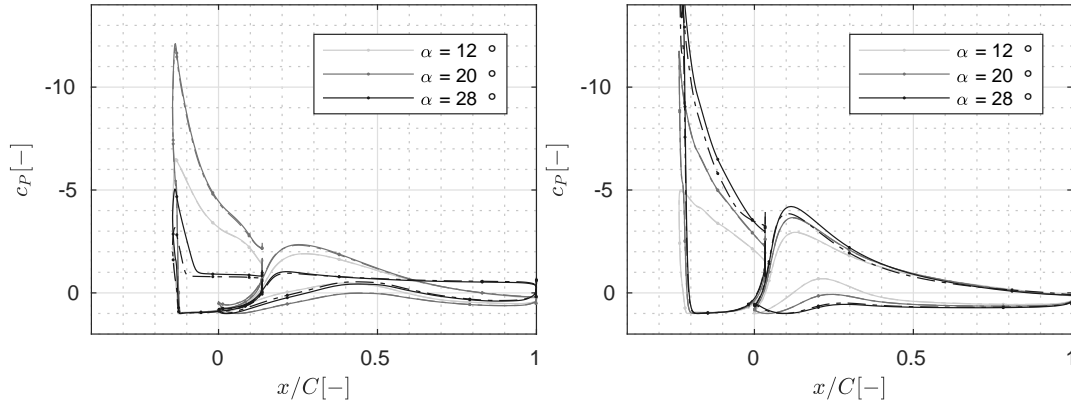
Figure 18. Pressure distribution from CFD for the clean ($-$) and the rough ($-.$) profile at different angles of attack for: **(a)** configuration C, and **(b)** configuration C*.

The pressure distributions for the profiles with the curtailed slat chord length are shown in Figure 18. The slat elements of these two profiles have the highest camber, the lowest thickness, and the highest slat angle when compared to designs obtained with the same optimization procedure. The interaction between all these partially counter-acting effects leads to the ~~lowest pressure near the trailing edge on the slat~~ highest suction peak on the main element and, as a consequence, the ~~highest suction peak on the main~~ lowest pressure near the trailing edge on the slat element when compared to all the other profiles with the same main element thickness. This holds true despite the slightly lower lift coefficients when sized up with all the other designs. Consequently, as compared to the other designs, the main element is producing a larger share of the overall lift loading. This explains why the pitching moment coefficients are significantly lower for the designs with the reduced chord length. Further, they also show the highest stall angles within the two categories. Given that, as shown in Figures B1 and B2, the stalling

mechanism is driven by the separation on the slat element, the reason for the higher stall angle could be the higher comparative circulation on the main element. This is because a higher circulation on the main element leads to a higher outflow velocity at the slat trailing edge, and hence, lower negative pressure gradients on the slat element.

Figure 19. Pressure distribution from CFD for the clean ($-$) and the rough ($-.$) profile at different angles of attack for: **(a)** configuration D and **(b)** configuration D*.

Finally, Figure 19 shows the pressure distributions for the two profiles with the thicker main element. As visible in Figure 13, due to the higher base profile thickness, these two profiles have the highest lift coefficients and the lowest aerodynamic efficiency pretty much at all investigated angles of attack. However, beyond $\alpha > 8°$, the pitching moment coefficients are roughly in the midfield between the highest values from the thinner designs with the regular slat chord length and the lower values from the thinner designs with the curtailed slat chord length. The origin of this is twofold. First, the pressure distributions show a slightly lower ratio of the slat to the main element lift loading for the designs with the thicker main element as compared to the other ones. Second, for the integral design case, the optimal slat placement is a bit further aft as compared to the other designs.

Some of the designs show very high suction peak values for the slat which is an indication that locally compressibility effects may not be negligible despite the low freestream Mach number of $Ma_\infty \approx 0.1$. Calculating the local Mach number from the incompressible flow field for all the CFD cases shows that for the designs and angle of attack configuration where the lift coefficient is higher than 4 the Mach number locally approaches 0.45. This is indeed very high and it is recommended that in future publications, compressibility effects should be considered if a design optimization for high lift is carried out. Nevertheless, given that the turbulence model of the CFD solver is expected to overpredict the stall angle, it is not certain that such high Mach numbers will actually be reached in real life.

4 Conclusions

460   This article ~~compromises~~ comprises a parametric study on both auxiliary and integral slat design for thick main elements at a Reynolds number of 10 million. For both the auxiliary and the integral design procedure the influence of changes in the optimization boundary conditions on the optimal design is investigated. Initially, a baseline design with a slat chord length of 40 % and a gap width of ~~8~~ 4 % of the chord length of the main element, as well as a 40 % thick main element is established. Subsequently, the influence of a 25 % reduction of the slat chord length, a 50 % decrease in the gap width and a 20 % increase

465   in the main element thickness on the optimal design is documented.

All of the obtained profiles are predicted to have higher lift coefficients at almost all positive angles of attack, delayed stall, less roughness sensitivity, higher glide ratios above angles of attack of about 8 degrees, high positive pitching moments and a steep lift drop beyond stall. These effects were more pronounced for the designs obtained with the integral design procedure, as opposed to the ones obtained with the auxiliary design procedure. Hence, from a purely aerodynamics driven point of view,

470   combined optimization of both elements offers additional advantages but also amplifies the caveats.

Comparison of the designs obtained with different boundary conditions gave rise to the following conclusions. While three out of the four investigated cases were carried out with a slat chord length of 40 %, a 30 % long slat element already offers many of the advantages of the two-element design without the caveat of a high positive pitching moment. While this comes at the expense of slightly lower lift coefficients, the stall angles are also higher. A reduction in the gap width did not offer any

475   benefits, but only two gap widths were investigated. Possibly, the sensitivity to this parameter warrants further investigation. Further, the increase in the stall angle and maximum glide ratio, as compared to the main element only, were more pronounced for the thicker main element. This indicates that this concept is more beneficial for thicker airfoils.

Summarizing, this article presented an analysis of the aerodynamic potential of slat elements for thick airfoils within the context of wind energy. Although this analysis highlights the benefits of a slat element on aerodynamic performance of wind

480   turbine airfoils, multiple aspects still need to be further investigated. From an aerodynamic point of view, the next step would be to investigate the influence of rotational effects. From a structural point of view, the next step would be to clarify how the significantly different aerodynamic performance would affect the structural design. The increase in the lift would allow a reduction of the chord length near the hub, which is beneficial for the standstill loads. However, it is still unclear how this would affect the scaling of the sectional bending and torsional stiffness, as well as, the blade mass. An increase in the box

485   length may also be necessary. In particular, the positive pitching moment may make the occurrence of an aeroelastic instability, such as divergence, more likely and the steep drop in lift post-stall may excite blade vibrations. Finally, logistics aspects such as the attachment of the slat to the main element also need further consideration.

Code and data availability. The open-source part of the codebase is available upon direct request with the correspondence author. Same goes for the data.

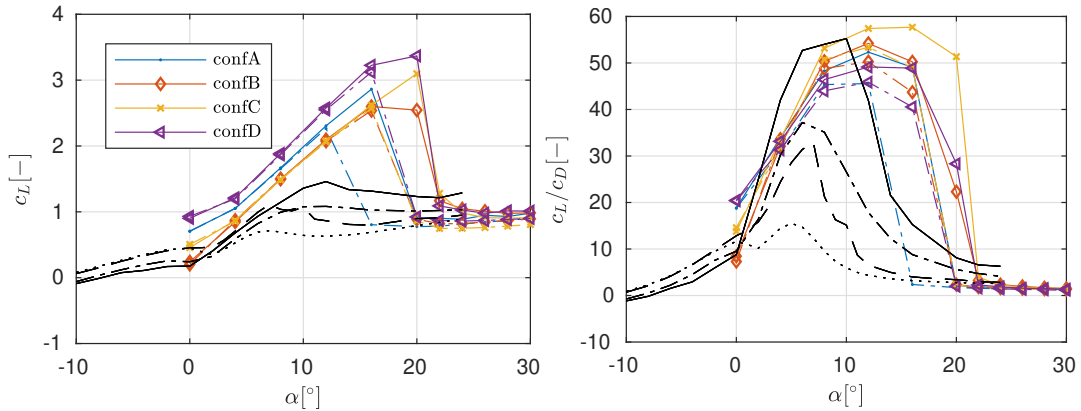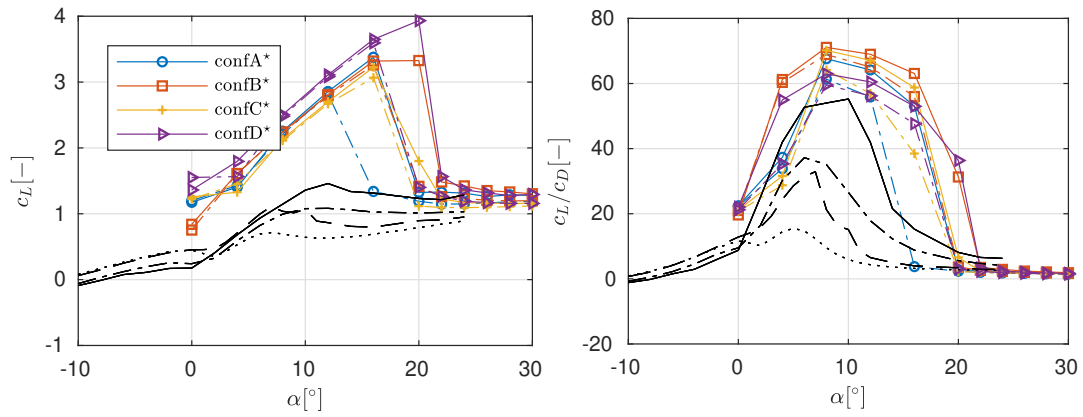**Appendix A: Designs optimized for maximum lift**

Figure A1. Lift **(a)** and glide ratio **(b)** polar from CFD for the slat configurations optimized for maximum lift using the auxiliary design strategy, the coefficients for the clean $(-)$ and tripped $(-.)$ DU40 profile only, as well as, the clean $(--)$ and tripped $(\cdot\cdot)$ FFA48 profile only are shown as well.

Figure A2. Lift **(a)** and glide ratio **(b)** polar from CFD for the slat configurations optimized for maximum lift using the integral design strategy, the coefficients for the clean (−) and tripped (−.) DU40 profile only, as well as, the clean (−−) and tripped (··) FFA48 profile only are shown as well.

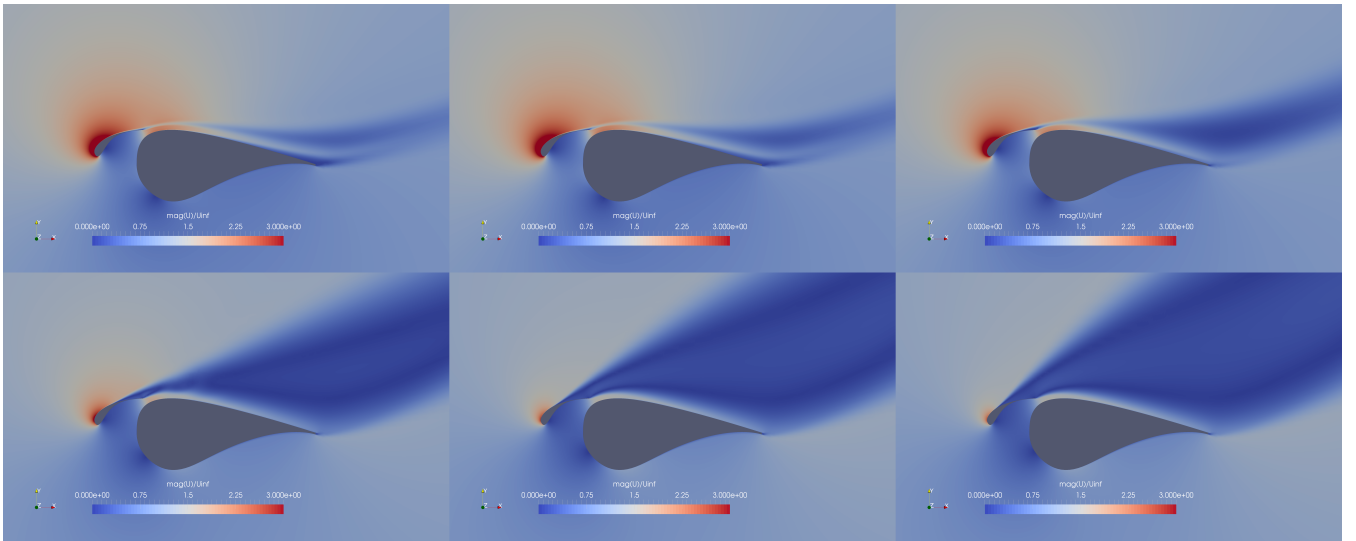505   **Appendix B: Stall mechanism on configuration C**

Figure B1. Flow fields around configuration C at the design Reynolds number and angles of attack ranging from $\alpha = 29°$ to $\alpha = 34°$ as predicted by CFD for the clean profile.
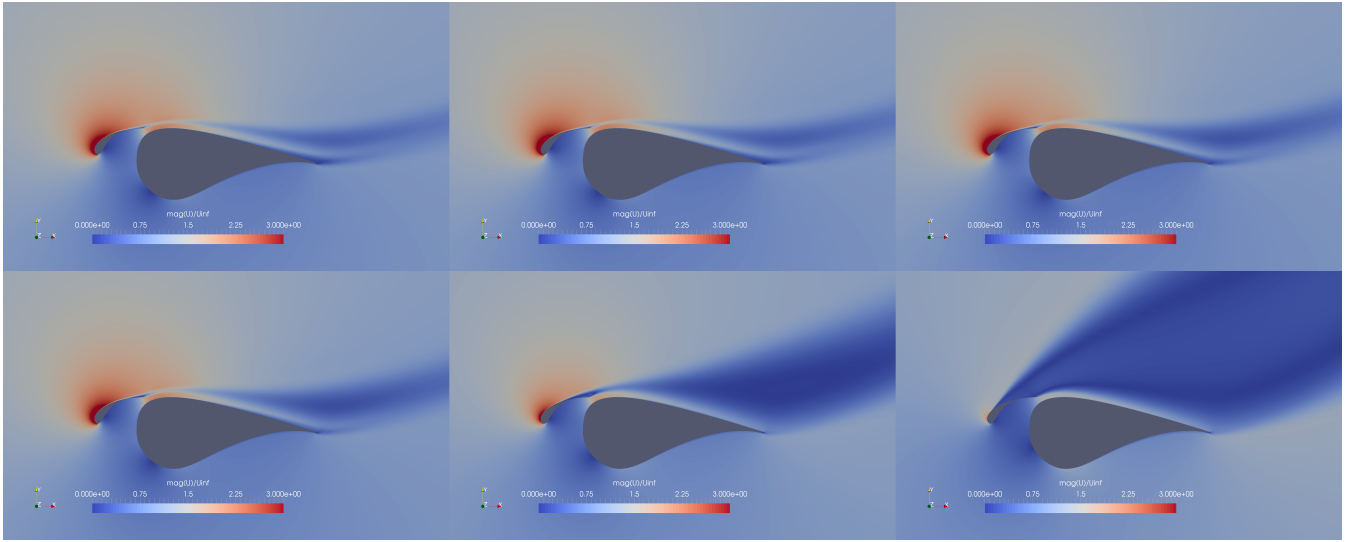
Figure B2. Flow fields around configuration C at the design Reynolds number and angles of attack ranging from $\alpha = 26°$ to $\alpha = 33°$ as predicted by CFD for the rough profile.

References

Bach, A., Lennie, M., Pechlivanoglou, G., Nayeri, C., and Paschereit, C.: Finite micro-tab system for load control on a wind turbine, Journal of Physics: Conference Series, 524, 012 082, https://doi.org/10.1088/1742-6596/524/1/012082, 2014.

515 Bach, A. B.: Gurney Flaps and Micro-Tabs for Load Control on Wind Turbines, Ph.D. thesis, Technische Universität Berlin, Fakultät für Verkehrs- und Machinensysteme, 2016.

Bak, C., Gaudern, N., Zahle, F., and Vronsky, T.: Airfoil design: Finding the balance between design lift and structural stiffness, Journal of Physics: Conference Series, 524, 012 017, https://doi.org/10.1088%2F1742-6596%2F524%2F1%2F012017, 2014.

Baldacchino, D., Manolesos, M., Ferreira, C., Salcedo, G., Aparicio, M., Chaviaropoulos, T., Diakakis, K., Florentie, L., García, N. R., Pa-
520 padakis, G., Sørensen, N. N., Timmer, N., Troldborg, N., Voutsinas, S., and van Zuijlen, A.: Experimental benchmark and code validation for airfoils equipped with passive vortex generators, Journal of Physics: Conference Series, 753, 022 002, http://stacks.iop.org/1742-6596/753/i=2/a=022002, 2016.

Carr, L. and Mc Alister, K.: The effect of a leading-edge slat on the dynamic stall of an oscillating airfoil, Aircraft Design and Technology Meeting, American Institute of Aeronautics and Astronautics, https://doi.org/10.2514/6.1983-2533, 1983.

525 Carr, L. W., Chandrasekhara, M. S., Wilder, M. C., and Noonan, K. W.: Effect of Compressibility on Suppression of Dynamic Stall Using a Slotted Airfoil, Journal of Aircraft, 38, 296–309, https://doi.org/10.2514/2.2762, 2001.

Choudhry, A., Arjomandi, M., and Kelso, R.: Methods to control dynamic stall for wind turbine applications, Renewable Energy, 86, 26 – 37, https://doi.org/https://doi.org/10.1016/j.renene.2015.07.097, 2016.

Deb, K., Pratap, A., Agarwal, S., and Meyarivan, T.: A fast and elitist multiobjective genetic algorithm: NSGA-II, IEEE Transactions on
530 Evolutionary Computation, 6, 182–197, https://doi.org/10.1109/4235.996017, 2002.

Drela, M.: A User's Guide to MSES 3.04. MIT Department of Aeronautics and Astronautics, http://web.mit.edu/drela/Public/web/mses/ (Accessed 01.08.2019).

Drela, M.: MISES Implementation of modified Abu-Ghanam/Shaw transition criterion, Report, MIT Aero-Astro, 1995.

Fouatih, O. M., Medale, M., Imine, O., and Imine, B.: Design optimization of the aerodynamic passive flow con-
535 trol on NACA 4415 airfoil using vortex generators, European Journal of Mechanics - B/Fluids, 56, 82 – 96, https://doi.org/https://doi.org/10.1016/j.euromechflu.2015.11.006, 2016.

Gaunaa, M., Zahle, F., Sørensen, N., and Bak, C.: Quantification of the Effects of Using Slats on the Inner Part of a 10MW Rotor, 2012.

Godard, G. and Stanislas, M.: Control of a decelerating boundary layer. Part 1: Optimization of passive vortex generators, Aerospace Science and Technology, 10, 181 – 191, https://doi.org/https://doi.org/10.1016/j.ast.2005.11.007, 2006.

540 Heine, B., Mulleners, K., Joubert, G., and Raffel, M.: Dynamic Stall Control by Passive Disturbance Generators, AIAA Journal, 51, 2086–2097, https://doi.org/10.2514/1.J051525, 2013.

Jonkman, J., Butterfield, S., Musial, W., and Scott, G.: Definition of a 5MW Reference Wind Turbine for Offshore System Development, National Renewable Energy Laboratory (NREL), https://doi.org/10.2172/947422, 2009.

Joubert, G., Le Pape, A., Heine, B., and Huberson, S.: Vortical Interactions Behind Deployable Vortex Generator for Airfoil Static Stall
545 Control, AIAA Journal, 51, 240–252, https://doi.org/10.2514/1.J051767, 2013a.

Joubert, G., Pape, A. L., Heine, B., and Huberson, S.: Deployable Vortex Generator Dynamic Stall Alleviation through Experimental and Numerical Investigations, Journal of the American Helicopter Society, 58, 1–13, https://doi.org/10.4050/jahs.58.032005, https://doi.org/10.4050/JAHS.58.032005, 2013b.

Langrty, R. and Menter, F. R.: Correlation-based transition modeling for unstructured parallelized computational fluid dynamics codes, AIAA
   550   Journal, 47, 2894–2906, 2009.

Liebeck, R. H.: Design of Subsonic Airfoils for High Lift, Journal of Aircraft, 15, 547–561, https://doi.org/10.2514/3.58406, 1978.

Manso Jaume, A. and Wild, J.: Aerodynamic Design and Optimization of a High-Lift Device for a Wind Turbine Airfoil, in: New Results
   in Numerical and Experimental Fluid Mechanics X, edited by Dillmann, A., Heller, G., Krämer, E., Wagner, C., and Breitsamter, C., pp.
   859–869, Springer International Publishing, Cham, 2016.

   555   Menter, F.: Two-Equation Eddy-Viscosity Turbulence Models for Engineering Applications, AIAA Journal, 32, 1598–1605,
   https://doi.org/10.2514/3.12149, 1994.

Moir, I.: Measurements on a Two-Dimensonal Aerofoil with High-Lift Devices, A Selection of Experimental Test Cases for the Validation
   of CFD Codes, volume II, AGARD ADVISORY REPORT NO 303, August 1993., 1993.

Mueller-Vahl, H., Pechlivanoglou, G., Nayeri, C. N., and Paschereit, C. O.: Vortex Generators for Wind Turbine Blades: A Combined Wind
   560   Tunnel and Wind Turbine Parametric Study, pp. 899–914, http://dx.doi.org/10.1115/GT2012-69197, 2012.

OpenFOAM-plus: version 1806, https://develop.openfoam.com/Development/OpenFOAM-plus (Accessed 01.08.2019).

Pape, A. L., Costes, M., Joubert, G., David, F., and Deluc, J.-M.: Dynamic Stall Control Using Deployable Leading-Edge Vortex Generators,
   AIAA Journal, 50, 2135–2145, https://doi.org/10.2514/1.J051452, 2012.

Pechlivanoglou, G. and Eisele, O.: Single and Multi-element Airfoil Performance Simulation Study and Wind Tunnel Validation, Wind
   565   Energy - Impact of Turbulence, Research Topics in Wind Energy 2, https://doi.org/10.1007/978-3-642-54696-9_3, 2014.

Pechlivanoglou, G., Nayeri, C., and Paschereit, C.: Fixed leading edge auxiliary wing as a performance increasing device for HAWT blades,
   2010.

Platypus: https://github.com/Project-Platypus/Platypus, documentation available at https://platypus.readthedocs.io/en/latest/index.html (Ac-
   cessed 01.08.2019).

   570   Rooij, R. and Timmer, W.: Roughness Sensitivity Considerations for Thick Rotor Blade Airfoils, 125, 2003.

Salcedo, S., Monge, F., Palacios, F., Gandía, F., Rodriguez-Sevillano, A., and Barcala, M.: Gurney flaps and trailing edge devices for wind
   turbines, 2, 1180–1186, 2006.

Schramm, M., Stoevesandt, B., and Peinke, J.: Simulation and Optimization of an Airfoil with Leading Edge Slat, Journal of Physics:
   Conference Series, 753, 022 052, http://stacks.iop.org/1742-6596/753/i=2/a=022052, 2016.

   575   Skinner, S.N. Zare-Behtash, H.: State-of-the-art in aerodynamic shape optimisation methods, Applied Soft Computing, 62, 933–962, 2018.

Smith, O. A. M.: High-Lift Aerodynamics, Journal of Aircraft, 12, 501–530, https://doi.org/10.2514/3.59830, 1975.

Sørensen, N. N.: Prediction of Multi Element Airfoils With the EllipSys Code, Tech. Rep. No. 1698(EN), Denmark Technical University,
   Risø, in T. Buhl (Ed.), Research inAeroelasticity EFP-2007-II (pp. 95-102)., 2009.

Storms, B. L. and Jang, C. S.: Lift enhancement of an airfoil using a Gurney flap and vortex generators, Journal of Aircraft, 31, 542–547,
   580   https://doi.org/10.2514/3.46528, 1994.

The DTU 10MW Reference Wind Turbine Project Site: http://dtu-10mw-rwt.vindenergi.dtu.dk, http://dtu-10mw-rwt.vindenergi.dtu.dk. Ac-
   cessed 01.08.2019.

van Dam, C. P., Chow, R., Zayas, J. R., and Berg, D. E.: Computational Investigations of Small Deploying Tabs and Flaps for Aerodynamic
   Load Control, Journal of Physics: Conference Series, 75, 012 027, http://stacks.iop.org/1742-6596/75/i=1/a=012027, 2007.

   585   van den Kieboom, K. Elham, A.: Combined Aerostructural Wing and High-Lift System Optimization, in: AIAA Aviation, 17-17 June 2016,
   Washington D.C., 17th AIAA/ISSMO Multidisciplinary Analysis and Optimization Conference, 2016.

29

Weick, F. E. and Noyes, R. W.: Wind tunnel research comparing lateral control devices, particularly at high angles of attack X : various control devices on a wing with a fixed auxiliary airfoil, Tech. Rep. NACA-TN-451, NASA, 1933.

Weick, F. E. and Wenziger, C. J.: The characteristics of a Clark Y wing model equipped with several forms of low-drag fixed slots, Tech. Rep. NACA-TR-407, NASA, 1933.

Zahle, F., Gaunaa, M., Sørensen, N., and Bak, C.: Design and Wind Tunnel Testing of a Thick, Multi-Element High-Lift Airfoil, European Wind Energy Association (EWEA), 2012.

590